

ASSEMBLY OF TWO-DIMENSIONAL ATOMIC LAYERS FOR QUANTUM
CIRCUIT ENGINEERING

A Dissertation

Presented to the Faculty of the Graduate School

of Cornell University

In Partial Fulfillment of the Requirements for the Degree of

Doctor of Philosophy

by

Kan-Heng Lee

December 2019

© 2019 Kan-Heng Lee

ASSEMBLY OF TWO-DIMENSIONAL ATOMIC LAYERS FOR QUANTUM
CIRCUIT ENGINEERING

Kan-Heng Lee, Ph. D.

Cornell University 2019

Ever since the first digital computer—built on hundreds of vacuum tubes—appeared in 1942, computers have evolved from room-sized machines to hand-held devices and transformed our daily lives. This impressive evolution in computers, the same as other modern technologies, is driven by the understanding of new physics, materials, and technologies. Undoubtedly, the next tech-revolution will depend on these likewise.

The Two-dimensional material family is one of the promising candidates for future technology. These materials include diverse material species from metals, semiconductors to super-conductors and so on, all with layered structures where each layer is only one to few atoms in thickness. Their structures of saturated in-plane covalent bonds result in the out-of-plane interlayer coupling via weak and directionless van der Waals force. These characteristics allow us to assemble any combination of two-dimensional materials layer-by-layer to create unprecedented heterostructures with atomic precision that can host exciting new physics.

In this dissertation, I will present my and my colleague's efforts to develop new methodologies for large-scale, layer-by-layer assembly of two-dimensional materials. These methods enable us to investigate and design the properties of the assembled films on the atomic scale. Based on our methods, we further demonstrate qubits that are built with two-dimensional materials for quantum computers for the first time. The methodologies and demonstrations here, hopefully, will help to pave the way for two-dimensional materials based technology in the future tech-revolution.

BIOGRAPHICAL SKETCH

Kan-Heng Lee was born in Taiwan. Grown up with parents who love to gift unassembled robot toys to their son for some unknown reason, he fell in love with building giant robots and machines. After he learned about outer space from the *discovery channel*, he has always told people that he wanted to build space elevators and go to the space in the future. In pursuit of this dream, he majored in Physics (, for some unknown reason like his parents,) at National Taiwan University and graduated Summa Cum Laude. In 2013, he went to the School of Applied and Engineering Physics at Cornell University and joined Prof. Jiwoong Park's group to pursue his Ph.D. There he studied and developed methodologies for two-dimensional materials for future nanotechnology. While unrelated to space elevators, he fell in love with the concept of building micro-, nano- and maybe one day angstrom-devices from bottom-up with atomic layers, which leads to this dissertation. He still might try something related to space elevators someday in the future, maybe built from bottom-up with atomic layers.

To my family and my little boy

ACKNOWLEDGMENTS

Learning to become a Ph.D. is a challenging task that is achievable only with many helps and supports from people around. First and foremost, I want to thank my advisor Prof. Jiwoong Park for the guidance and inspiration during my Ph.D. studies. Standing at the front of new science and technology is frustrating because ninety-nine percent of the days are filled with only failures. Jiwoong has been offering insights from my failures, and pushing me for innovation when I pulled back because of frustrations. Besides knowledge, this mindset of persistence is what I appreciate the most and will undoubtedly benefit my career and life alike.

I would like to thank my other two committee members, Prof. Paul McEuen and Prof. Lena Kourkoutis. Paul gave the most inspiring course in my life when I took his *Solid State Physics* class in 2013. Later in a private chat, he told me that he believed the best scientist is the one with the most curiosity, and his words have encouraged me through the years whenever I got lazy and wanted to get pass with a question. Lena is a great mentor and scientist. She cares about the career of her students. She has also brought many interesting scientific questions to me that eventually change my angle of thinking.

Park group members come-and-go all the time, but I always love this group because people are supportive in work and in life as a big family. In particular, I need to thank two important people who have led me to what I am today. Dr. Robin Havener was my first mentor and she taught me all the knowledge in nano-fabrication, which became the foundation of this dissertation. Dr. Kibum Kang then guided me through one of my proudest work, published in *Nature*, from forming ideas to designing experiments to paper writing. Also many thanks to all the other members Wei, Lola, Lujie, Saien, Yimo, Cheol-Joo, Fai, Yui, Marcos, Lei, Long, Hui, Chibeom, Preeti, Joonki, Yu, Kim, Fauzia, Josh, Baorui, Andy, Andrew, Jong Hoon, and Myungjae.

During my Ph.D. research, there were many collaborations that were so meaningful and inspiring that led me to my next career plan. Among them, I have to specifically thank three people – Prof. David Schuster, Dr. Srivatsan Chakram, and Dr. Brian Zhou, all at the University of Chicago. They brought to me the challenges ‘Can we do this with two-dimensional materials?’ and have since worked closely with me and taught me the knowledge of quantum computing and quantum sensing.

Lastly, I want to thank my parents, sister and my wife. I believe Ph.D. starts on the date I was born, and the road to this moment is paved throughout my life with the help of their unconditional supports. Thank you is not enough to describe my feelings.

This acknowledgment is probably longer than the graduate school would like, but this is indeed how much favor one would need to complete a Ph.D. degree.

TABLE OF CONTENTS

BIOGRAPHICAL SKETCH.....	iv
DEDICATION	v
ACKNOWLEDGEMENTS	vi
TABLE OF CONTENTS	viii
LIST OF FIGURES	x
LIST OF TABLES	xii
CHAPTER ONE: Overview of Two-Dimensional Materials.....	1
1.1. <i>Introduction</i>	1
1.2. <i>From 3D to 2D Materials</i>	3
1.3. <i>From 2D materials to 3D Artificial Solids</i>	6
1.4. <i>Large Scale Synthesis of 2D Materials</i>	9
1.5. <i>Overview of The Dissertation</i>	12
1.6. <i>References</i>	14
CHAPTER TWO: Layer-By-Layer Assembly of Two-Dimensional Materials into Wafer-Scale Heterostructures	20
2.1. <i>Introduction</i>	20
2.2. <i>Programmed Vacuum Stacking</i>	21
2.3. <i>Characterizations of the Wafer-Scale Layer-By-Layer Assembled films</i>	24
2.4. <i>Band Engineering of Tunnel Junctions</i>	28
2.5. <i>Freestanding Ultrathin Film for Optical and Mechanical Applications</i>	31
2.6. <i>Summary</i>	33
2.7. <i>Appendix</i>	34
2.8. <i>References</i>	38
CHAPTER THREE: Quantum Confined Stark Effect in Twisted Bilayer Graphene	40
3.1. <i>Introduction</i>	40
3.2. <i>Method of Simultaneous Electrical and Optical Characterizations</i>	42
3.3. <i>Quantum Confined Stark Effect in Twisted Bilayer Graphene</i>	45
3.4. <i>Many-Body Interactions in Twisted Bilayer Graphene</i>	48
3.5. <i>Summary</i>	50
3.6. <i>Appendix</i>	51
3.7. <i>References</i>	52
CHAPTER FOUR: Two-Dimensional Material Tunnel Barrier for Josephson	

Junctions and Superconducting Qubits.....	57
4.1. <i>Introduction.....</i>	57
4.2. <i>The Barrier-First Method.....</i>	59
4.3. <i>Tunable Josephson Current via Layer-by-Layer Assembly.....</i>	62
4.4. <i>MoS₂ Superconducting Qubits.....</i>	66
4.5. <i>Summary.....</i>	70
4.6. <i>Appendix.....</i>	71
4.7. <i>References.....</i>	71
CHAPTER FIVE: Future Directions and Perspectives.....	80
5.1. <i>Future Directions.....</i>	80
5.2. <i>Ongoing Works.....</i>	82
<i>Two-dimensional polymer for Layer-by-Layer Assembly.....</i>	82
<i>Foldable 3D Integrated Atomically-Thin Circuitry.....</i>	84
<i>High Coherence MoS₂ Quantum Electronics.....</i>	86
5.3. <i>Final Thoughts.....</i>	86
5.4. <i>References.....</i>	87

LIST OF FIGURES

Figure 1.1 Two-dimensional material family	1
Figure 1.2 Physical properties of graphene	4
Figure 1.3 Direct to indirect gap in MoS ₂	5
Figure 1.4 Band offsets and gaps of different TMDs	6
Figure 1.5 Van der Waals heterostructures	8
Figure 1.6 Chemical vapor deposition of graphene	10
Figure 1.7 MOCVD growth of TMD monolayers.....	12
Figure 2.1 Programmed vacuum stacking.....	22
Figure 2.2 Characterization of the assembled films	25
Figure 2.3. Band Engineering of Tunnel Junctions.....	29
Figure 2.4 Large-scale free standing TMD films	32
Figure A2.1 Optical absorption spectra of N_L -MoS ₂ films	34
Figure A2.2 Uniform Raman properties of PVS-stacked MoS ₂ films	34
Figure A2.3 High yield of mechanical peeling	35
Figure A2.4 Dark-field optical microscope imaging	36
Figure A2.5 Additional $50 \times 50 \mu\text{m}^2$ AFM images	36
Figure A2.6 Interlayer coupling in PVS-stacked bilayer WS ₂	37
Figure A2.7 Additional electrical characterization.....	37
Figure 3.1 Experimental set-up	41
Figure 3.2 Simultaneous electrical and optical measurements.....	43
Figure 3.3 Quantum confined Stark effect	47
Figure 3.4 Many-body interactions	49
Figure A3.1 Process for making twisted bilayer graphene with controlled twist angle	51
Figure A3.2 Color plots for the interlayer optical resonance peak line shape	51
Figure A3.3 Log-log plot of ΔEA as a function of D	52
Figure A3.4 Single particle band structure of tBLG under electric field	52
Figure 4.1. Schematics of the structure of a Josephson junction.....	57
Figure 4.2 The barrier-first method	60
Figure 4.3 Electrical characterization and Josephson effect	63
Figure 4.4 A superconducting qubit with a MoS ₂ tunnel barrier	67

Figure A4.1 SEM image of the suspended airbridge	71
Figure A4.2. Normalized dI/dV curves of 2L and 3L-MoS ₂ barrier as a function of V	71
Figure 5.1 Laminar assembly polymerization and hybrid heterostructures.	83
Figure 5.2 Foldable 3D integrated atomically-thin circuitry	86

LIST OF TABLES

Table I List of our combined characterizations and their length scales	24
--	----

CHAPTER ONE

Overview of Two-Dimensional Materials

1.1. Introduction

The discovery of the first 2D materials occurred in an unexpectedly simple way. Kostya Novoselov and Andre Geim put graphite, which can be found in a pencil, on a piece of Scotch tape and just repetitively attached and peeled the two halves of the tape. After a few times of attach-and-peel, they looked under various microscopes to see what happened to the graphite. What they found was *graphene*¹ (Figure 1.1a). Being a mere single layer of carbon atoms in a honeycomb lattice with all atoms having complete covalent bonds, graphene is free of bonding in the out-of-plane direction and hence named the first 2D material. It's so simple that anyone can do it in an elementary school art class, but the influence of graphene in both science and technology has won Kostya Novoselov and Andre Geim the Nobel Prize in physics in

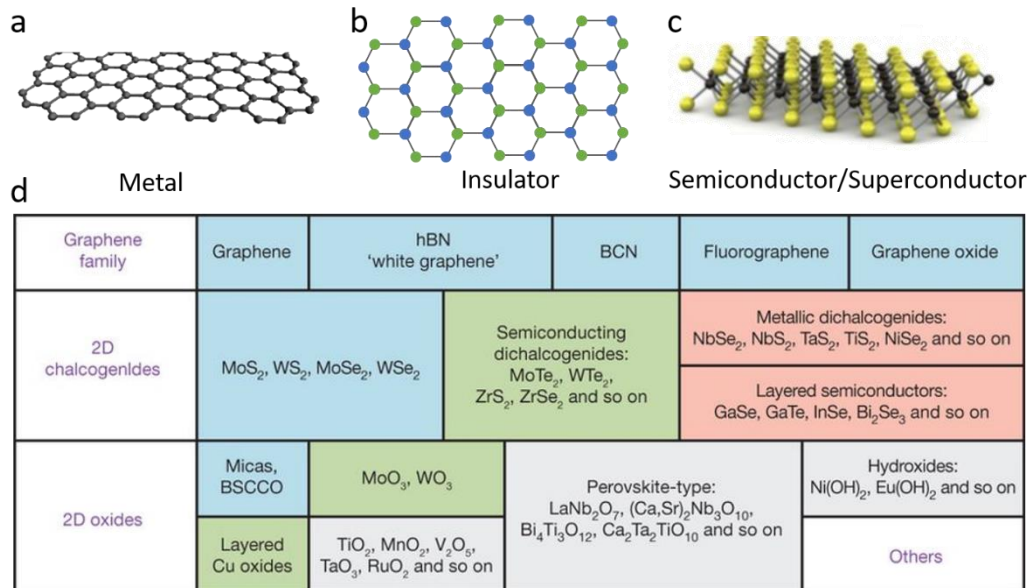


Figure 1.1 Two-dimensional material family. **a-c**, schematics of graphene, hexagonal boron nitride and transition metal dichalcogenides. The schematics of transition metal dichalcogenides is reproduced from [5]. **d**, summary of 2D materials, reproduced from [7].

2010, ‘for groundbreaking experiments regarding the two-dimensional material graphene.’²

Ever since then, many more 2D materials such as hexagonal boron nitride (hBN) and transition metal dichalcogenides (TMDs) are similarly exfoliated using the Scotch tape method, leading to a large 2D material family that includes diverse material properties from metals, insulators, semiconductors to more complex ones like superconductors and topological insulators (Figure 1.1 b-d)^{1,3-7}. In addition, as the monolayers of 2D materials interact with the surrounding primarily through van der Waals interactions, different 2D materials can be assembled without constraints common in conventional growth techniques, such as lattice matching. This gives ways to generate previously inaccessible heterostructures. With all these favorable characteristics, numerous physics phenomena are discovered or revisited in this new two-dimensional world; some examples are fractional quantum Hall effect, valley Hall effect, and more recently exciton condensation at high temperature⁸⁻¹⁰.

Despite the great success of exfoliation using scotch tape, the small sample size, typically only a few micrometers, limits the use of 2D materials to scientific proof-of-concept demonstrations. In 2009, chemical vapor deposition (CVD) for large area growth of uniform, high-quality, monolayer graphene was introduced by the Ruoff group and was also used by other groups to grow hBN^{11,12}. In 2015, our group introduced metal-organic chemical vapor deposition (MOCVD) for growing high mobility TMD monolayers on the wafer scale¹³. In 2017, our group further developed a technique for wafer-scale layer-by-layer assembly of 2D material monolayers with nearly pristine interlayer interfaces¹⁴. These developments for generating high-quality 2D materials and their heterostructures on the large scale are critical steps, as they brought 2D materials into a technologically relevant scale without sacrificing the excellent properties observed in exfoliated samples. With such quality and scalability,

previous proof-of-concept demonstrations using 2D materials, such as valleytronics¹⁵ and one nanometer transistors¹⁶, could become feasible for future technology.

In this chapter, only the basic knowledge necessary to understand this dissertation will be introduced, in the simplest way. General and detailed introduction to 2D materials can be found elsewhere⁴⁻⁶.

1.2. From 3D to 2D Materials

The bulk form of a 2D material has a layered structure where the layers are held together by van der Waals interaction. As the thickness (i.e., number of layers) of 2D materials gets below the quantum limit, loosely speaking five nanometers, the material properties could be drastically different from those of the bulk. For example, they become thin enough to be effectively controlled by electrostatic gating. In addition, the crystal symmetry can disappear or emerges as the number of layers changes. Such changes result in intriguing physics and properties in 2D materials. Here, we will particularly discuss two material systems central to this dissertation: graphene and TMDs.

Graphene, a single layer of carbon atoms arranged in a honeycomb lattice, has a hexagonal reciprocal lattice, where the energy-momentum dispersion is linear at the six corners, forming the Dirac cones (Figure 1.2a)^{17,18}. The charge neutrality point of graphene sits where the top and bottom cones meet, which results in the low conductance of intrinsic graphene due to the vanishing density of states at this point. The Fermi level of graphene can be easily shifted away from the charge neutrality point through electrostatic gating, and the carrier concentration can be tuned over a few order of magnitude¹⁹. The high tunability of the Fermi level enables the control of electrical conductance (Figure 1.2b⁴), optical absorption (Figure 1.2c²⁰) and many other properties, making it one of the most versatile platforms to test physics at

different regime.

Transition metal dichalcogenides are layered materials in the form of MX_2 , where M is a transition metal element (e.g. Mo, W, Nb, etc.) and X is a chalcogen group element (S, Se, Te). Unlike graphene, monolayers of TMDs are bi-elemental and three-atom thick (Figure 1.1c). This results in more complex variations in crystal symmetry that give rise to the abundant physics in TMDs such as the valley Hall effect. In addition, with the large number of elements in both transition metal and chalcogen groups, TMDs include a wide variety of materials from semiconductors, like MoS_2 , WSe_2 , to superconductors like NbSe_2 . Here, we will specifically focus on the semiconducting TMDs, as the large scale synthesis of other types of TMD monolayers remains a challenge at this time.

In 2010, Kin Fai Mak and Andrea Splendiani independently investigated and

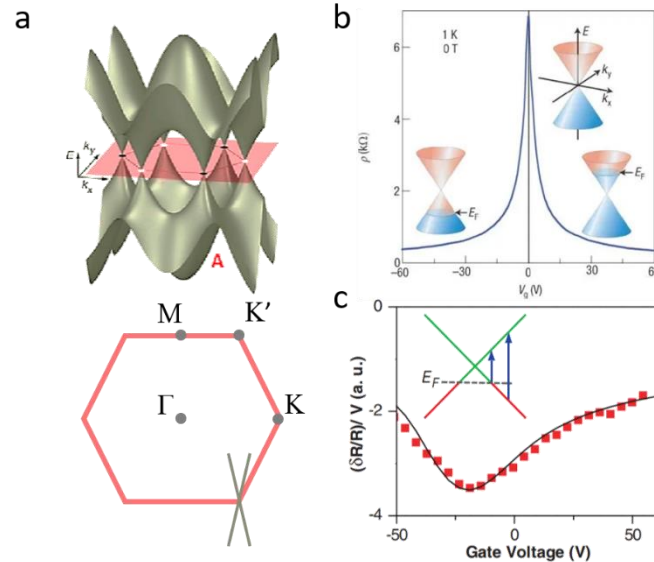


Figure 1.2 Physical properties of graphene. **a**, schematics of graphene band structure (top, reproduced from [18]) and the cross section at the charge neutrality point (bottom). Γ , M, K, K' are the high symmetry points. One of the Dirac cones is shown at the bottom right corner. **b**, Electrical gate tunable resistivity of graphene. (inset) corresponding fermi level for each gate voltage. Reproduced from [4]. **d**, Optical response (here reflection contrast) as a function of gate voltage, reproduced from [20].

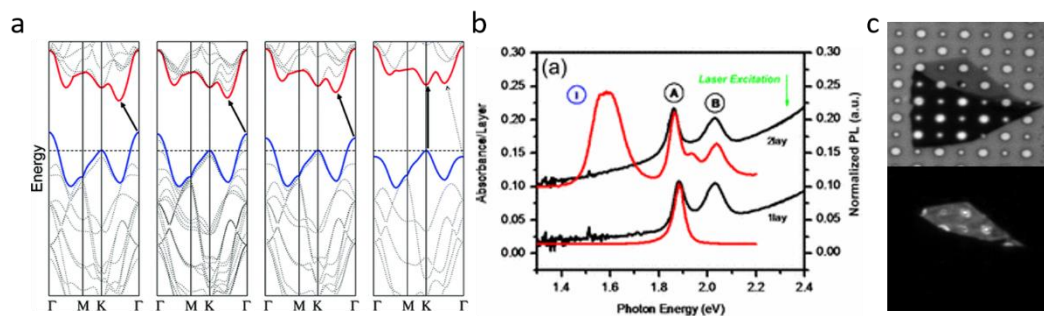


Figure 1.3 Direct to indirect gap in MoS₂. **a**, band structures of (left to right) bulk, four-layer, two-layer and monolayer MoS₂. The black arrows indicate the transition from valence band maximum to conduction band minimum. Reproduced from [22]. **b**, Optical absorption (black) and photoluminescent (red) spectra of two-layer and monolayer MoS₂. A and B denotes the excitonic peaks and I is the indirect gap peak. **c**, (top) optical image and (bottom) photoluminescent image of an exfoliated MoS₂ flake containing both monolayer and two-layer region. **b** and **c** are reproduced from [21].

reported the properties of MoS₂ when the number of layers is reduced down to the monolayer limit (Figure 1.3a)^{21,22}. MoS₂ is a semiconductor with an indirect bandgap of 1.3 eV in the bulk form, but the bandgap is enlarged as the number of layers is decreased and can be up to ~1.9 eV for monolayers. Moreover, the indirect bandgap transitions into a direct gap when MoS₂ is thinned from bilayer to monolayer, resulting in a sharper absorption edge at the bandgap energy and a more than 100-fold increase in photoluminescence quantum yield for the monolayers (Figure 1.3b and c). This indirect-to-direct gap transition are also reported for other typical semiconducting TMDs such as MoSe₂ and WS₂ except for WSe₂, which was recently shown to have an indirect gap even for monolayer²³.

The atomic thinness of semiconducting TMD monolayers results in the reduced screening of Coulomb interaction between quasiparticles. Such strong interactions lead to abundant many-body physics, which can be studied via photoluminescent spectra. For example, tightly bound excitons (i.e., electron-hole pair) with binding energies as large as a few hundred meV are measured²⁴⁻²⁶. Electrostatic gating

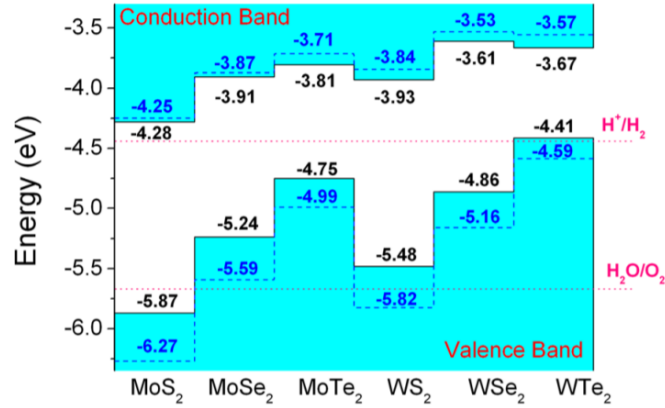


Figure 1.4 Band offsets and gaps of different TMDs. Reproduced from [29].

can further control the charge density in the semiconducting TMDs, allowing other complex many-body interactions such as tightly bound trions and the quantum-confined Stark effect to be realized^{27,28}. Hence, excitons and the photoluminescence of semiconducting TMD monolayers have become one of the most important characterization methods for probing the physical properties in these materials.

In addition, these semiconducting TMDs possess different semiconductor properties such as the bandgap and band offsets, as summarized in Figure 1.4²⁹. The variation between different semiconducting TMDs allows them to be used for different purposes. For example, a larger bandgap TMD can be used as 2D dielectric¹⁴, while a smaller bandgap TMD such as MoTe₂ can be used for infrared detectors and photodiodes³⁰. The various band offsets, on the other hand, offer a diverse toolset to generate heterostructures with the band structures engineered layer-by-layer, as will be discussed in the following section.

1.3. From 2D materials to 3D Artificial Solids

Monolayers of 2D materials interact with the environment only through the weak and directionless van der Waals interaction. As no chemical bonding is formed between the layers, different 2D materials can be arbitrarily assembled together

without the constraints of the composition nor lattice matching/alignment as illustrated in Figure 1.5a⁷. In other words, with N different 2D materials, N^L different structures can be designed for an assembly of L monolayers. For example, by counting the 2D materials that are readily available ($N \sim 10$) and an assembly of five monolayers that can be easily achieved nowadays, up to 100,000 different structures can be created. Note here we have only counted the different compositions in the structures and no other variables. The versatility and designability of the assembly of 2D materials into 3D artificial crystal allows unprecedented heterostructures to be constructed, providing a powerful platform that has attracted much attention across multiple scientific fields. In a review article⁷, Andre Geim described his prospectives and visions regarding building such exciting 3D artificial solids, which were named van der Waals heterostructures. In addition, he made an analogy between 2D material assembly and the toy LEGO to emphasize the designability of this method.

However, the analogy with LEGO doesn't completely capture the characteristics of 2D material assembly, as LEGO blocks have to be assembled in specific directions while 2D materials can be assembled with rotation between the layers owing to the directionless van der Waals interactions. As illustrated in Figure 1.5b, assembly of 2D materials is closer to stacking paper, where the paper can be stacked together with any interlayer rotation. (Each color presents a different 2D materials.) This interlayer rotation can significantly change the characteristics of the as-fabricated van der Waals heterostructures. For instance, it was recently demonstrated that when two graphene monolayers, which are semi-metallic, are stacked with an interlayer rotation of 1.1° to form twisted bilayer graphene (tBLG), the tBLG becomes a superconductor with a critical temperature up to 1.7 K (Figure 1.5c)³¹. In another case, the dielectric constant of MoS₂ multilayers with and without interlayer rotation is found to be up to three times different¹⁴.

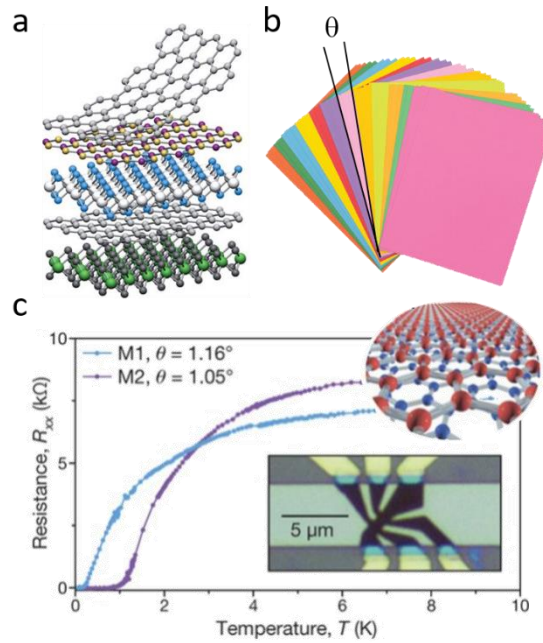


Figure 1.5 Van der Waals heterostructures. **a**, schematics of a van der Waals heterostructure. Reproduced from [7]. **b**, an analogy to assembly of 2D materials is the stacking of color paper, where each color represents a 2D material. A random, finite rotation θ between each paper is allowed. **c**, superconductivity in twisted bilayer graphene with a twist angle θ of ~ 1.1 . (top inset) schematics of twisted bilayer graphene; (bottom inset) optical image of the device. Reproduced from [31].

Van der Waals heterostructures bring an even more complex test ground for physics such as the excitonic effect in semiconducting TMDs. For example, it has been demonstrated that the excitons generated in a $\text{MoSe}_2\text{-WSe}_2$ heterostructure can have the electrons and holes spatially separated in different layers, resulting in an order of magnitude longer lifetime for interlayer excitons compared to that of intralayer excitons³². The coupling strength between the two semiconducting TMDs can be further varied by inserting layers of hBN in between as atomically thin spacer³³. This prevents the interlayer exciton recombination and was recently demonstrated to serve as a promising method for observing high temperature exciton condensation¹⁰.

1.4. Large scale synthesis of 2D materials

The abundant physics in both 2D material monolayers and their heterostructures presents a great opportunity for both scientific research as well as technological applications. However, the sample size of 2D material monolayers prepared by exfoliation of the bulk crystal is typically only a few micrometers despite the excellent sample quality. Because scalability is critical for technological applications, it is essential to synthesize 2D materials monolayer on the large scale while maintaining the material properties close to those of exfoliated samples. Here, we will briefly discuss the chemical vapor deposition (CVD) method for graphene and TMDs, which produces high quality monolayers of 2D materials on the large scale. It is noted that there are other large scale synthesis methods such as sulfurization of transition metal thin films and liquid exfoliation, each of which has different advantages for technological applications such as cost-efficiency.

Chemical vapor deposition for graphene

CVD growth has emerged as one of the most prevailing methods for the synthesis of high quality, large scale graphene monolayers since 2008^{11,34}. In this method, methane and hydrogen gas is introduced into a hot furnace at around 1000°C, and the graphene can be synthesized on catalytic metal substrates, typically Ni or Cu. Different metal substrates may have different growth mechanisms, and thus it is crucial to use the appropriate metal substrates for graphene. For instance, graphene grown on a Ni substrate tends to have more multilayer coverage, because the carbon decomposed from methane is first dissolved into Ni and then precipitate to the surface to form graphene as in Figure 1.6a^{34,35}. On the other hand, Cu has a much lower solubility for carbon, and therefore the formation of graphene on Cu is mainly a surface reaction. This growth mechanism is a self-limiting process, meaning the reaction is stopped once the Cu surface is covered by graphene (Figure 1.6b). The self-

limiting growth allows graphene grown on a Cu substrate to be mainly single layer, and is the most common way to grow graphene monolayer nowadays. Graphene CVD growth is also compatible with the industrial roll-to-roll process, which allows the production of graphene for industrial use³⁶.

Besides the growth mechanism, the crystallinity of the metal substrate can play an important role for graphene growth. Typical CVD-grown graphene is polycrystalline, where each grain can have a random orientation. As the lattice orientation becomes important in determining the interlayer rotation in the vertical assembly of 2D materials, a growth method that allows graphene to have a single lattice orientation is desired. For this, our group demonstrated a graphene growth on

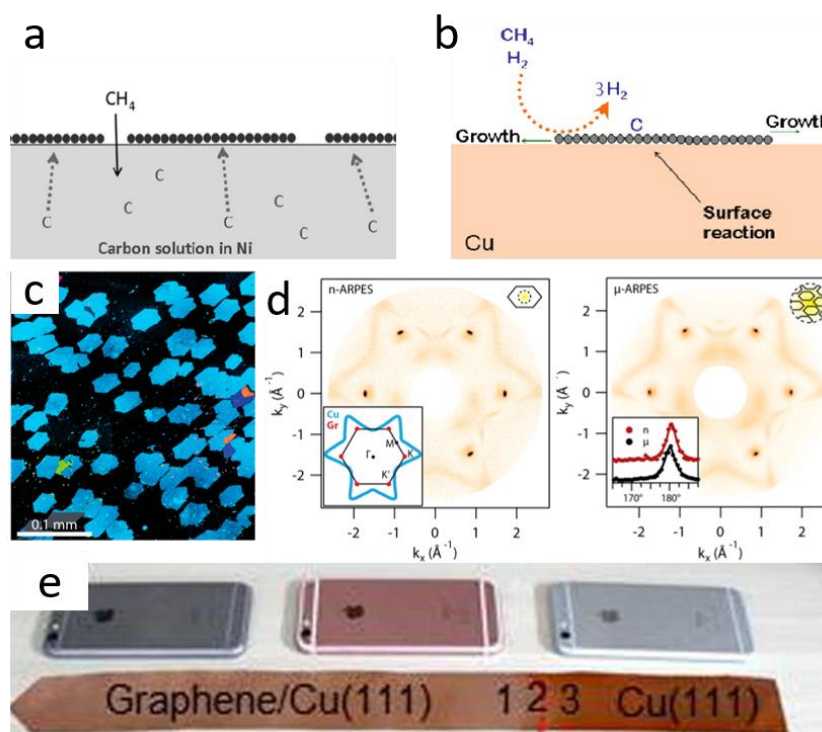


Figure 1.6 Chemical vapor deposition of graphene. **a-b**, schematics of graphene CVD growth on Ni and Cu substrates. Reproduced from [35]. **c**, Dark-field TEM image of aligned graphene grown on Cu (111). The colors indicate the lattice orientations. **d**, ARPES data measured with a 200 nm (left) and a 90 μm photon spot, which are showing the same electronic structure. Both **c** and **d** are reproduced from [37]. **e**, Large scale aligned graphene growth. Reproduced from [38].

the Cu (111) surface that is polycrystalline but has near single crystalline structure and electronic properties³⁷. In this method, the Cu (111) surface is used as a template for the grains of graphene to be aligned in one direction, which can be confirmed by the dark-field transmission electron microscope (TEM) image shown in Figure 1.6c. The angle-resolved photoemission spectroscopy (ARPES) in Figure 1.6d further confirms that this aligned graphene shows an electronic band structure similar to that of single crystalline graphene. As further demonstrated in Figure 1.6e, this method of growing highly-oriented graphene on the Cu (111) surface has recently been demonstrated up to a $5 \times 50 \text{ cm}^2$ area in a single, twenty minutes growth, making it close to the scale suitable for industrial use³⁸.

Metal-organic chemical vapor deposition for TMD monolayers

The metal-organic chemical vapor deposition (MOCVD) method for growing TMD monolayers on the large scale was first introduced by our group in 2015, which has brought this large group of 2D materials into the technologically-relevant scale similar to the first large-scale graphene CVD growth¹³. Early CVD growths of TMDs, which typically used solid phase precursors such as MoO_3 and S for MoS_2 , only provided uniform monolayer coverage of around a few millimeters⁴¹. One major issue for the solid phase precursor is that the vapor pressure can vary over time, making the precursor flow during growth difficult to control. By using highly volatile metal-organic precursors, such as $\text{Mo}(\text{CO})_6$ with $(\text{C}_2\text{H}_5)_2\text{S}$ for MoS_2 , the MOCVD method allows the uniform flow of the precursors, where the concentrations can be precisely controlled using mass-flow controllers during growth (Figure 1.7). With such controllability of the growth environment, we were able to grow MoS_2 , WS_2 , MoSe_2 , WSe_2 on silicon oxide substrates up to four-inch wafer scale. The TMD monolayers grown by the MOCVD method exhibit excellent mobility of $\sim 30 \text{ cm}^2 \text{ V}^{-1} \text{ s}^{-1}$ for MoS_2 , which is close to those measured from exfoliated samples. High quality, large

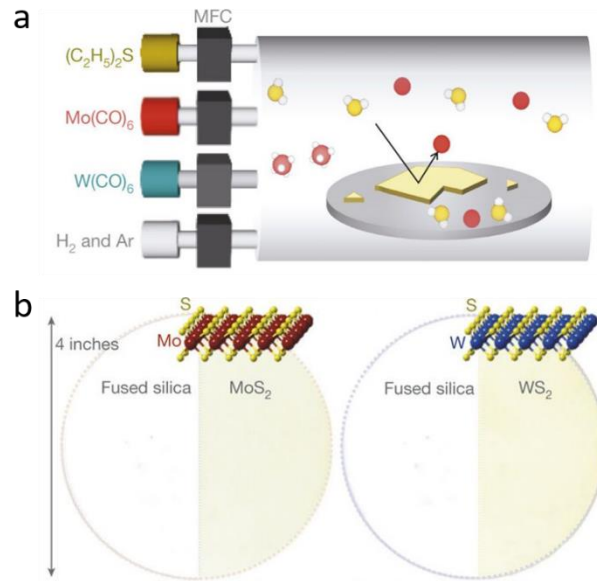


Figure 1.7 MOCVD growth of TMD monolayers. **a**, schematics of the MOCVD growth. **b**, Photos of MoS₂ and WS₂ grown on 4-inch fused silica wafer. The left half of each photo is a photo of blank fused silica for color contrast. (inset) schematics of the crystal structure of MoS₂ and WS₂. All figures are reproduced from [13].

scale TMD monolayers are essential for practical applications of the material as well as the assembly of 2D materials on the large scale. Hence, TMD monolayers grown by the MOCVD method will be the primary source of TMDs used in this dissertation.

1.5. Overview of the Dissertation

While many exciting physics has been discovered and demonstrated with 2D materials and their heterostructures, most of them remain proof-of-conception experiments due to the small scale of the samples and devices. Without scalability, most of these exciting discoveries and promising applications will likely stay as knowledge instead of becoming technologies that can advance human life. As such, this dissertation have been dedicated to scaling up the process for 2D materials while maximally preserving the intrinsic properties of 2D materials. Another important goal for my Ph.D. research was realizing 2D material-based quantum electronics that takes

advantages of the sequential layer-by-layer assembly of 2D materials to achieve atomic scale designability of vertical structures of devices, on the wafer scale, too.

This dissertation presents the efforts of our group toward these goals. In Chapter 2, we demonstrated a wafer-scale vacuum-stacking method, called programmed vacuum stacking (PVS), that enables the layer-by-layer assembly of 2D material monolayers with excellent spatial uniformity and pristine interlayer interfaces. The PVS method allows us to address the challenges to generate high quality van der Waals heterostructures on the large scale, which is the foundation for the later work of building quantum electronics using 2D materials. This work was published in *Nature* (2017). In Chapter 3, the optical and electrical properties of artificially-stacked twisted bilayer graphene are studied. Here, we grow centimeter scale aligned graphene and stack them on top of each other with a controlled angle, which allows us to form a uniform twisted angle over a large area. We look at the optical transition that arose from the van Hove singularities where the Dirac cones from each graphene monolayer intercept. This optical transition is excitonic, and we were able to control the optical response through different doping and electric field on the twisted bilayer graphene. Our study reveals the quantum-confined Stark effect and many-body interactions in this system. In Chapter 4, we demonstrated, for the first time, MoS₂ superconducting qubits, where the Josephson energies can be tuned via the number of layers of MoS₂ assembled for the tunnel barrier of Josephson junctions. This allows Josephson junctions and superconducting qubits to access the diverse material properties of 2D materials, offering a new material systems for studying and engineering novel quantum circuit elements for quantum computing in the future. This work was published in *Nano Letters* (2019). Chapter 5 presents the potential future directions for the above projects, as well as a brief introduction to some of the exciting work currently going on in our group. The dissertation will be concluded with my

personal perspective on the topic of 2D materials at the end.

1.6. References

1. Novoselov, K. S., Geim, A. K., Morozov, S. V., Jiang, D., Zhang, Y., Dubonos, S. V., Grigorieva, I. V. & Firsov, A. A. Electric Field Effect in Atomically Thin Carbon Films. *Science* **306**, 666–669 (2004).
2. The Nobel Prize in Physics 2010. NobelPrize.org. Nobel Media AB 2019. Thu. 31 Oct 2019. *NobelPrize.org* (2010). at <https://www.nobelprize.org/prizes/physics/2010/summary/>
3. Novoselov, K. S., Jiang, D., Schedin, F., Booth, T. J., Khotkevich, V. V., Morozov, S. V. & Geim, A. K. Two-dimensional atomic crystals. *Proc. Natl. Acad. Sci. U. S. A.* **102**, 10451–10453 (2005).
4. Geim, A. K. & Novoselov, K. S. The rise of graphene. *Nat. Mater.* **6**, 183–191 (2007).
5. Wang, Q. H., Kalantar-Zadeh, K., Kis, A., Coleman, J. N. & Strano, M. S. Electronics and optoelectronics of two-dimensional transition metal dichalcogenides. *Nat. Nanotechnol.* **7**, 699–712 (2012).
6. Kou, L., Ma, Y., Sun, Z., Heine, T. & Chen, C. Two-Dimensional Topological Insulators: Progress and Prospects. *J. Phys. Chem. Lett.* **8**, 1905–1919 (2017).
7. Geim, A. K. & Grigorieva, I. V. Van der Waals heterostructures. *Nature* **499**, 419–425 (2013).
8. Bolotin, K. I., Ghahari, F., Shulman, M. D., Stormer, H. L. & Kim, P. Observation of the fractional quantum Hall effect in graphene. *Nature* **462**, 196–199 (2009).

9. Mak, K. F., McGill, K. L., Park, J. & McEuen, P. L. The valley Hall effect in MoS₂ transistors. *Science* **344**, 1489–1492 (2014).
10. Wang, Z., Rhodes, D. A., Watanabe, K., Taniguchi, T., Hone, J. C., Shan, J. & Mak, K. F. Evidence of high-temperature exciton condensation in two-dimensional atomic double layers. *Nature* **574**, 76–80 (2019).
11. Li, X., Cai, W., An, J., Kim, S., Nah, J., Yang, D., Piner, R., Velamakanni, A., Jung, I., Tutuc, E., Banerjee, S. K., Colombo, L. & Ruoff, R. S. Large-Area Synthesis of High-Quality and Uniform Graphene Films on Copper Foils. *Science* **324**, 1312–1314 (2009).
12. Kim, G., Jang, A.-R., Jeong, H. Y., Lee, Z., Kang, D. J. & Shin, H. S. Growth of High-Crystalline, Single-Layer Hexagonal Boron Nitride on Recyclable Platinum Foil. *Nano Lett.* **13**, 1834–1839 (2013).
13. Kang, K., Xie, S., Huang, L., Han, Y., Huang, P. Y., Mak, K. F., Kim, C.-J., Muller, D. & Park, J. High-mobility three-atom-thick semiconducting films with wafer-scale homogeneity. *Nature* **520**, 656–660 (2015).
14. Kang, K., Lee, K.-H., Han, Y., Gao, H., Xie, S., Muller, D. A. & Park, J. Layer-by-layer assembly of two-dimensional materials into wafer-scale heterostructures. *Nature* **550**, 229–233 (2017).
15. Schaibley, J. R., Yu, H., Clark, G., Rivera, P., Ross, J. S., Seyler, K. L., Yao, W. & Xu, X. Valleytronics in 2D materials. *Nat. Rev. Mater.* **1**, 1–15 (2016).
16. Desai, S. B., Madhvapathy, S. R., Sachid, A. B., Llinas, J. P., Wang, Q., Ahn, G. H., Pitner, G., Kim, M. J., Bokor, J., Hu, C., Wong, H.-S. P. & Javey, A. MoS₂ transistors with 1-nanometer gate lengths. *Science* **354**, 99–102 (2016).

17. Castro Neto, A. H., Guinea, F., Peres, N. M. R., Novoselov, K. S. & Geim, A. K. The electronic properties of graphene. *Rev. Mod. Phys.* **81**, 109–162 (2009).
18. Wang, J., Xu, X., Mu, X., Ma, F. & Sun, M. Magnetism and spintronics on two-dimensional composite materials of graphene/hexagonal boron nitride. *Mater. Today Phys.* **3**, 93–117 (2017).
19. Mak, K. F., Sfeir, M. Y., Wu, Y., Lui, C. H., Misewich, J. A. & Heinz, T. F. Measurement of the Optical Conductivity of Graphene. *Phys. Rev. Lett.* **101**, 196405 (2008).
20. Wang, F., Zhang, Y., Tian, C., Girit, C., Zettl, A., Crommie, M. & Shen, Y. R. Gate-Variable Optical Transitions in Graphene. *Science* **320**, 206–209 (2008).
21. Mak, K. F., Lee, C., Hone, J., Shan, J. & Heinz, T. F. Atomically Thin MoS₂: A New Direct-Gap Semiconductor. *Phys. Rev. Lett.* **105**, 136805 (2010).
22. Splendiani, A., Sun, L., Zhang, Y., Li, T., Kim, J., Chim, C.-Y., Galli, G. & Wang, F. Emerging Photoluminescence in Monolayer MoS₂. *Nano Lett.* **10**, 1271–1275 (2010).
23. Hsu, W.-T., Lu, L.-S., Wang, D., Huang, J.-K., Li, M.-Y., Chang, T.-R., Chou, Y.-C., Juang, Z.-Y., Jeng, H.-T., Li, L.-J. & Chang, W.-H. Evidence of indirect gap in monolayer WSe₂. *Nat. Commun.* **8**, 1–7 (2017).
24. He, K., Kumar, N., Zhao, L., Wang, Z., Mak, K. F., Zhao, H. & Shan, J. Tightly Bound Excitons in Monolayer $\{\mathrm{WSe}\}_2$. *Phys. Rev. Lett.* **113**, 026803 (2014).
25. Chernikov, A., Berkelbach, T. C., Hill, H. M., Rigosi, A., Li, Y., Aslan, O. B., Reichman, D. R., Hybertsen, M. S. & Heinz, T. F. Exciton Binding Energy and

- Nonhydrogenic Rydberg Series in Monolayer WS_2 . *Phys. Rev. Lett.* **113**, 076802 (2014).
26. Ugeda, M. M., Bradley, A. J., Shi, S.-F., da Jornada, F. H., Zhang, Y., Qiu, D. Y., Ruan, W., Mo, S.-K., Hussain, Z., Shen, Z.-X., Wang, F., Louie, S. G. & Crommie, M. F. Giant bandgap renormalization and excitonic effects in a monolayer transition metal dichalcogenide semiconductor. *Nat. Mater.* **13**, 1091–1095 (2014).
27. Mak, K. F., He, K., Lee, C., Lee, G. H., Hone, J., Heinz, T. F. & Shan, J. Tightly bound trions in monolayer MoS₂. *Nat. Mater.* **12**, 207–211 (2013).
28. Roch, J. G., Leisgang, N., Froehlicher, G., Makk, P., Watanabe, K., Taniguchi, T., Schönenberger, C. & Warburton, R. J. Quantum-Confined Stark Effect in a MoS₂ Monolayer van der Waals Heterostructure. *Nano Lett.* **18**, 1070–1074 (2018).
29. Kang, J., Tongay, S., Zhou, J., Li, J. & Wu, J. Band offsets and heterostructures of two-dimensional semiconductors. *Appl. Phys. Lett.* **102**, 012111 (2013).
30. Zhu, Y., Li, Z., Zhang, L., Wang, B., Luo, Z., Long, J., Yang, J., Fu, L. & Lu, Y. High-Efficiency Monolayer Molybdenum Ditelluride Light-Emitting Diode and Photodetector. *ACS Appl. Mater. Interfaces* **10**, 43291–43298 (2018).
31. Cao, Y., Fatemi, V., Fang, S., Watanabe, K., Taniguchi, T., Kaxiras, E. & Jarillo-Herrero, P. Unconventional superconductivity in magic-angle graphene superlattices. *Nature* **556**, 43–50 (2018).
32. Rivera, P., Schaibley, J. R., Jones, A. M., Ross, J. S., Wu, S., Aivazian, G., Klement, P., Seyler, K., Clark, G., Ghimire, N. J., Yan, J., Mandrus, D. G., Yao, W.

- & Xu, X. Observation of long-lived interlayer excitons in monolayer MoSe₂–WSe₂ heterostructures. *Nat. Commun.* **6**, 6242 (2015).
33. Fang, H., Battaglia, C., Carraro, C., Nemsak, S., Ozdol, B., Kang, J. S., Bechtel, H. A., Desai, S. B., Kronast, F., Unal, A. A., Conti, G., Conlon, C., Palsson, G. K., Martin, M. C., Minor, A. M., Fadley, C. S., Yablonovitch, E., Maboudian, R. & Javey, A. Strong interlayer coupling in van der Waals heterostructures built from single-layer chalcogenides. *Proc. Natl. Acad. Sci.* **111**, 6198–6202 (2014).
34. Yu, Q., Lian, J., Siriponglert, S., Li, H., Chen, Y. P. & Pei, S.-S. Graphene segregated on Ni surfaces and transferred to insulators. *Appl. Phys. Lett.* **93**, 113103 (2008).
35. Zhang, Y., Zhang, L. & Zhou, C. Review of Chemical Vapor Deposition of Graphene and Related Applications. *Acc. Chem. Res.* **46**, 2329–2339 (2013).
36. Kidambi, P. R., Mariappan, D. D., Dee, N. T., Vyatskikh, A., Zhang, S., Karnik, R. & Hart, A. J. A Scalable Route to Nanoporous Large-Area Atomically Thin Graphene Membranes by Roll-to-Roll Chemical Vapor Deposition and Polymer Support Casting. *ACS Appl. Mater. Interfaces* **10**, 10369–10378 (2018).
37. Brown, L., Lochocki, E. B., Avila, J., Kim, C.-J., Ogawa, Y., Havener, R. W., Kim, D.-K., Monkman, E. J., Shai, D. E., Wei, H. I., Levendorf, M. P., Asensio, M., Shen, K. M. & Park, J. Polycrystalline Graphene with Single Crystalline Electronic Structure. *Nano Lett.* **14**, 5706–5711 (2014).
38. Xu, X., Zhang, Z., Dong, J., Yi, D., Niu, J., Wu, M., Lin, L., Yin, R., Li, M., Zhou, J., Wang, S., Sun, J., Duan, X., Gao, P., Jiang, Y., Wu, X., Peng, H., Ruoff,

R. S., Liu, Z., Yu, D., Wang, E., Ding, F. & Liu, K. Ultrafast epitaxial growth of metre-sized single-crystal graphene on industrial Cu foil. *Sci. Bull.* **62**, 1074–1080 (2017).

CHAPTER TWO

Layer-By-Layer Assembly of Two-Dimensional Materials into Wafer-Scale Heterostructures

2.1. Introduction

Modern technologies for precisely designing the vertical composition of the semiconductor films on the atomic scale provide the foundation for modern integrated circuitry and novel materials discovery¹⁻³. The existing methods for generating such films, such as chemical vapor deposition, pulsed laser deposition, and molecular beam deposition, generally rely on the direct sequential growth, where one layer of material is deposited directly on top of the previous one. While the thickness and composition of the resulting films can be controlled down to the atomic scale using this approach, the growth dynamics of one material are often sensitive to the previously deposited one that also serves as the growth substrate, making additional tuning and customization necessary, especially for heterostructure films.

With the discovery of 2D materials, a new approach for realizing such precisely-designed films has been proposed based on the sequential layer-by-layer assembly. Here, 2D material monolayers are used as atomically-thin building blocks, which can be vertically stacked on top of another through van der Waals interactions⁴⁻⁶. As no interlayer bonding is formed, the addition of a new layer is mostly independent of the previous layers, hence making such an approach advantageous for realizing previously inaccessible heterostructures with novel physical properties⁷⁻¹¹. However, there has been no large-scale assembly method that maintained the intrinsic properties of these heterostructures while producing pristine interlayer interfaces¹²⁻¹⁵, which limits the use of this concept to only small-size proof-of-concept

¹All work in this chapter has been published in *Nature*, **550**, 229–233(2017), DOI:10.1038/nature23905

²Kan-Heng Lee and Dr. Kibum Kang contributed equally to this work.

demonstrations using exfoliated samples (, usually size of a few μm).

In this chapter, we report the wafer-scale semiconductor films whose vertical composition and properties are directly designed on the atomic scale using layer-by-layer assembly of 2D material monolayers, which are shown to have excellent spatial uniformity and pristine interfaces. We use the newly-developed method, named programmed vacuum stacking, where a series of wafer-scale, three-atom-thick semiconductors (MoS_2 , MoSe_2 , and WS_2) are stacked under vacuum. Using our approach, we fabricate a variety of large-scale high-quality heterostructure films and devices that were previously inaccessible. These include superlattice films having composition vertically-designed layer-by-layer, batch-fabricated tunnel device arrays with their resistance tuned over four orders of magnitude, band-engineered heterostructure tunnel diodes, and millimeter-scale ultrathin membranes and windows. In addition, these stacked films are highly detachable and compatible with water or plastic surface, which will enable their integration with advanced optical and mechanical systems and applications in unconventional environments.

2.2. Programmed Vacuum Stacking

Figure 2.1a schematically illustrates the process of our newly-developed Programmed Vacuum Stacking (PVS): **I**, wafer-scale 2D monolayers are synthesized individually using MOCVD¹⁶. **II**, the initial layer $L0$, spin-coated with an adhesive polymer film, is mechanically peeled from the growth substrate (SiO_2/Si) using a thermal release tape (TRT). **III**, $L0/TRT$ is then stacked and pressed on top of the next layer $L1$ (on the growth substrate) in a vacuum chamber, forming an air-free interface between $L0$ and $L1$. **IV**, $L1/L0/TRT$ is peeled off from the substrate. The vacuum stack (**III**) and peel (**IV**) steps are repeated to directly program the vertical composition of the film with the desired number of layers (N_L). **V**, the N_L -layer film is then released

from the *TRT* onto a target substrate, in either supported or suspended form.

Figure 2.1b-c shows a representative high-quality semiconductor heterostructure film generated using the PVS process. The film is assembled by vertically stacking nine layers of individual wafer-scale monolayer transition metal dichalcogenide (TMD) films alternating between MoS₂ and WS₂ (see schematic in Figure 2.1b). The scanning transmission electron microscopy (STEM) data in Figure 2.1c confirm that its composition is vertically designed with atomic-scale precision and clean interfaces. First, five dark layers and four bright layers are clearly visible in the cross-sectional annular dark field (ADF) STEM image of the film (Figure 1c left panel), which correspond to the five MLs of MoS₂ and four MLs of WS₂, respectively. The chemical composition of each layer is directly confirmed by electron energy loss spectroscopy (EELS; Figure 2.1c right panel), which shows the Mo peaks only for the MoS₂ layers, but a uniform S signal everywhere within the film. Second, all nine

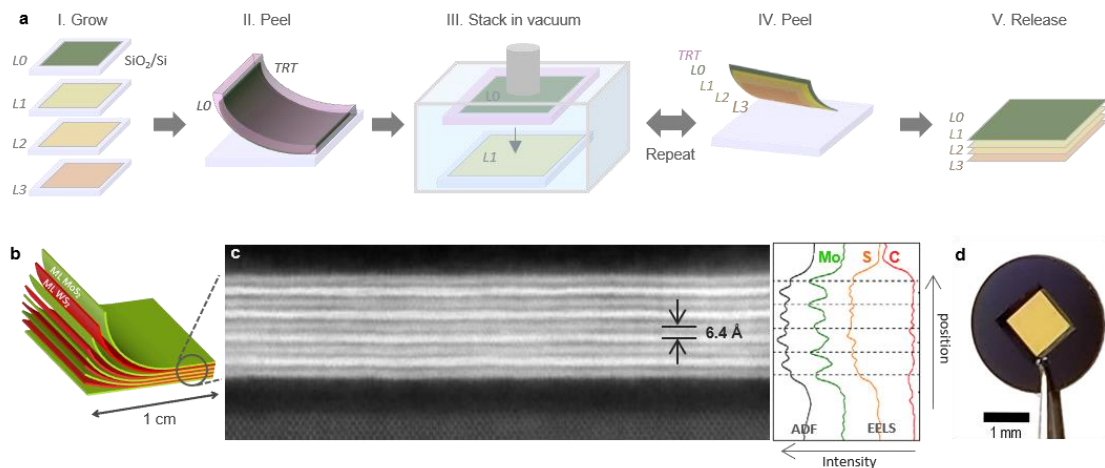


Figure 2.1 Programmed vacuum stacking. **a**, a schematic for the PVS process. See main text for a detailed description. **b**, schematic diagram of a vertically stacked MoS₂/WS₂ superlattice. **c**, left: a cross-sectional ADF STEM image of a superlattice film transferred on a SiO₂/Si substrate. The bright and dark layers are WS₂ and MoS₂ MLs, respectively, with the Si crystal lattice shown at the bottom; right: intensity profiles measured from the ADF STEM image and the EELS mapping along the out-of-plane direction. black - ADF STEM; green - EELS for Mo; orange - EELS for S; red - EELS for C. **d**, photo of a large-scale freestanding ultrathin semiconductor film (7-layer MoS₂; thickness ~ 5nm). It is fully suspended over a 1 × 1mm² hole on a TEM chip.

individual layers appear uniform and continuous, and run straight and parallel to each other. The interfaces between adjacent layers remain clean and free of bubbles or wrinkles, with a constant interlayer distance of 0.64 nm, which is consistent with the value expected for MoS₂/WS₂ with a non-zero interlayer rotation angle¹⁷. Third, the EELS data further shows a very low signal for carbon (red curve, Figure 2.1c) within the film near the detection limit of our instrument. Additional STEM images and EELS spectra of more heterostructure films are shown in Figure 2.2d. In Figure 2.1d, we further demonstrate that the as-generated film can be completely separated from the substrate as an ultrathin freestanding film. Here, another high-quality large-scale semiconductor film assembled with seven layers of MoS₂ is suspended over a 1 × 1 mm² square hole in the middle of a TEM chip. This freestanding film is thinner than 5 nm, hence results in one of the highest aspect ratios (length/thickness ~ 0.2 million) ever reported for freestanding semiconductor films¹⁸⁻²⁰. Achieving a high aspect ratio also indicates that our film has excellent structural quality and mechanical strength. Altogether, the data in Figure 2.1 demonstrate that our PVS process has produced high-quality detachable semiconductor films with atomic-scale programmability and pristine interfaces.

The PVS process provides a key advantage over existing methods of layer-by-layer assembly: a wafer-scale process that maintains pristine interlayer interfaces of the as-fabricated film. For the wafer-scale process, the MOCVD process is used to grow homogeneous wafer-scale semiconductor monolayers as the building blocks, here MoS₂, MoSe₂, and WS₂ as demonstrated. For the pristine interlayer interfaces, we optimize the synthesis to generate excellent surface properties, allowing these building blocks to be cleanly peeled off from the growth substrates without the use of any etchants or solvents. These building blocks are then assembled under vacuum using a customized apparatus for wafer-scale vacuum-stacking. As we show below, this

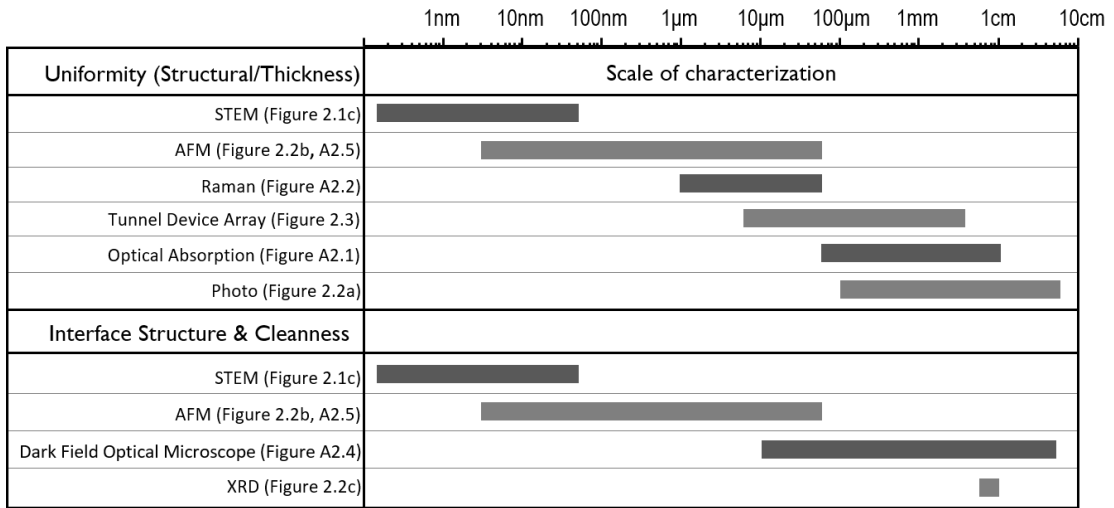


Table I. List of our combined characterizations and their length scales. Here, the left end of each bar indicates the resolution of the technique, and the right end indicates the largest field of view.

greatly improves the interface quality and flatness of the films, minimizing the amount of amorphous carbon or trapped air at the interfaces. Moreover, the PVS process are set to be used with an arbitrary 2D material as long as its adhesion to the stacked film is stronger than that to the growth substrate, making this a general approach for producing large-scale, vertically-designed stacked films with pristine interfaces.

2.3. Characterizations of the Wafer-Scale Layer-By-Layer Assembled films

In this section, we utilize several characterization tools to confirm the key advantage of the PVS process claimed above. Because the defects can be extremely small down to nanometer while our film is as large as several inches, spanning over seven orders of magnitudes in the length scale, we use multiple characterization techniques in combination as summarized in Table I.

First, we confirm that our stacked films are spatially uniform. Figure 2.2a displays photos of a three-layer MoS₂ film taken during the process. The figure shows a 2" round region of LO after the initial peeling (left image), and a three-layer MoS₂

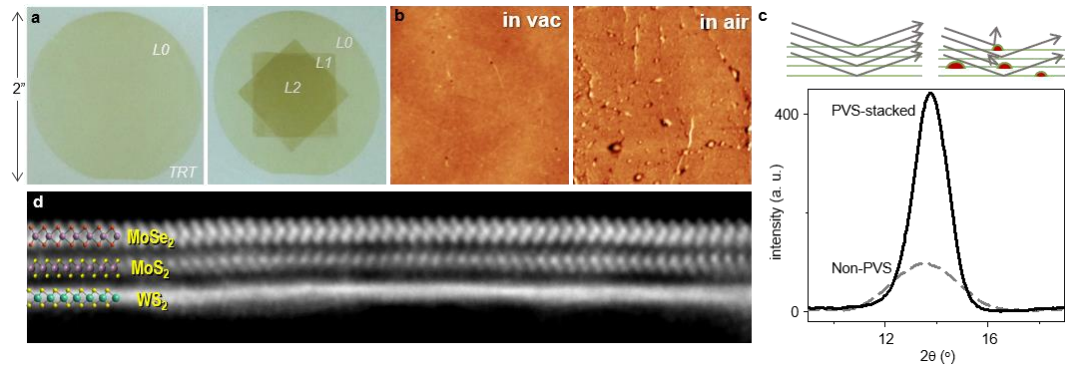


Figure 2.2 Characterization of the assembled films. **a**, photos of wafer-scale MoS₂ films after step **II** (left image), where the first layer (*L0*) on *TRT* is peeled from a 2” wafer, and after step **IV** (right image), where two more layers *L1* and *L2* (1” squares) are stacked on *L0*, forming a 3L MoS₂ film. **b**, AFM height images (2 μm × 2 μm) taken from the bottom (*L2*) side of 3L-MoS₂ films stacked in vacuum (top right) and air (bottom left). The film stacked in vacuum shows a flatter surface without bubble-like structure. Height scales: ±5nm. **c**, XRD pattern of 4L-MoS₂ generated by the PVS process (solid curve) and conventional dry transfer (dashed curve). The single peak at 2θ~14° is originated from X-ray beams diffracted by MLs spaced along the *c*-axis direction. Upper inset: schematics of the X-ray diffraction from stacked films with pristine interfaces (left) and contaminated interfaces (right). The effective beam area used for the measurement is an ellipse of 0.5 × 1 cm². **d**, cross-sectional STEM image of a MoSe₂/MoS₂/WS₂ film with the electron beam aligned with the zig-zag axis of MoSe₂ (top) and MoS₂ (middle).

film (right image) after two 1” squares of MoS₂ MLs, *L1* and *L2*, are subsequently stacked. All layers remain continuous and uniform in these photos, where each pixel is estimated to have a resolution of few hundreds by hundreds μm². Optical absorption spectra (see Figure A2.1 in 2.7. *Appendix*) up to ten layers further demonstrate that there are no significant spatial variations in the optical absorption down to tens of μm. In Figure A2.2, Raman mapping using the E_{2g}^1 peak of MoS₂ also shows spatially homogeneous peak frequency for different numbers of layers of MoS₂, further confirming the uniformity of our films with a resolution down to a micrometer. The uniformity directly results from the uniform monolayers grown by MOCVD (~99.5% monolayer coverage as shown in Ref.16) and the nearly perfect yield of our PVS process that allows each wafer-scale monolayer to be completely separated from the

growth substrate and transferred to the stacked film. This nearly perfect yield is evidenced by the residue-free growth substrates after MoS₂ monolayers are peeled off, as shown using the scanning electron microscopy and Raman measurements of the substrates (Figure A2.3).

Second, we confirm that our stacked films show greatly improved interlayer structures and flatness, which is critical to the quality and sub μm scale homogeneity of the film. Figure 2.2c presents the thin film X-ray diffraction (XRD) data measured from a PVS-stacked 4L-MoS₂ film (solid curve) over a 0.5 by 1 cm² sample area. It shows a peak at $2\theta \sim 14^\circ$ coming from the X-ray diffraction by the monolayers spaced along the c-axis direction. The intensity of this peak is five-times higher than that observed from the other film generated by a non-PVS process (dashed curve; conventional dry-transfer¹³), indicating a significantly improved layered structure in the former. In addition, the peak position can be converted to an average interlayer spacing of 0.64 nm, close to the expected value of 0.65 nm calculated for twisted MoS₂ multilayers¹⁷. The above results indicate that the PVS process indeed improves the coherence of interlayer structure over a centimeter scale, suggesting cleaner interfaces with a reduced amount of interlayer contaminations in the films (schematic, Figure 2.2c). Dark field optical microscopy (Figure A2.4) also shows that the number of scatterers is reduced by 98% over a 5 by 5 mm² area in PVS-stacked films, confirming the significantly improved film flatness. Furthermore, Figure 2.2b shows the atomic force microscopy (AFM) images (measured on the bottom side of L2) of two MoS₂ films ($N_L = 3$), whose preparation steps are identical except for the stacking environment: one is stacked in vacuum (left), and the other in air (right). The film stacked in vacuum (roughness ~ 270 pm) is much smoother than the one stacked in air (roughness ~ 700 pm). In addition, the vacuum-stacked film is free of bubble-like features, which are clearly visible in the film stacked in air, and are similar to the

features reported in previous works¹⁴⁻¹⁵. Additional AFM images (Figure A2.5) show similar improvements up to 50 by 50 μm^2 areas.

As our films are generated by stacking monolayers, they show random interlayer rotations as a result of the directionless Van der Waals interactions. This random interlayer rotation is in contrast to the naturally-grown multilayers 2D materials, which typically show either aligned lattice (i.e. no rotation) or some specific rotation angles that have the commensurate structures. This is directly demonstrated in Figure 2.2d with the cross-sectional STEM image of a $\text{MoSe}_2/\text{MoS}_2/\text{WS}_2$ film. Here, the zig-zag axes of the MoSe_2 (top) and MoS_2 (middle) layers are roughly parallel to the electron beam while that of WS_2 is not. Additionally, in stark contrast to other layer-by-layer growth techniques as mentioned in the introduction of this chapter, this image directly shows that the vertical stacking is successful in the presence of a lattice mismatch (*e.g.* MoSe_2 lattice constant is larger than MoS_2 by $\sim 4.2\%$)²¹ or an interlayer rotation (between MoS_2 and WS_2). This interlayer rotation is an important characteristic of layer-by-layer assembled 2D materials, which contributes to many interesting new phenomena such as the one shown below. The entire Chapter 3 will be dedicated to this topic with twisted bilayer graphene.

As an example, one consequence of the interlayer rotation in our TMD multilayer films is the changes in exciton properties, as demonstrated in Figure A2.6 with the stacked $2L\text{-WS}_2$. Here, we use the MOCVD-grown monolayer flakes, where each flake is typically single crystalline. The interlayer rotation angle θ can then be approximated using the orientation of the edges of the triangles as shown in the optical image of Figure A2.6a. Figure A2.6b (main panel) first shows that the PL measured from a $2L\text{-WS}_2$ region is strongly quenched compared to the PL from a monolayer region. The bilayer PL spectra also show two additional peaks (see inset) that correspond to the indirect peak (peak I) and interlayer exciton peak (peak A_I)²². The

PL quenching and the presence of I peak indicate the direct-to-indirect bandgap transition due to the interlayer coupling in WS₂. Figure A2.6c schematically illustrates the origin of the A_I peak, which occurs when an exciton is generated across different layers of twisted 2L-WS₂. The peak line-shape analysis further shows the angle-dependence of I, A, and A_I peak energies as in Figure A2.6e (left), demonstrating the effect of interlayer rotation on the exciton characteristic in the stacked films. Similar results and the detailed explanation are also reported using as-grown twisted bilayer WS₂ (, duplicated in Figure A2.6e (right), ref. 22).

2.4. Band Engineering of Tunnel Junctions

The layer-by-layer assembly allows for the generation of a large number of distinct, vertically-designed semiconductor films with only a small set of 2D materials. For example, with n different 2D materials, one can construct n^L distinct films by stacking L layers. Here, the n different 2D materials can be individually grown without considering the specific stacking sequence, making the programming process simple and straightforward. Moreover, these stacked films would enable batch-fabrication of electronic and optoelectronic devices as the PVS process generates homogenous structures and properties over large areas.

In Figure 2.3, we demonstrate these by generating a series of distinct stacked films and heterostructures that have a larger number of stacked interfaces, all assembled with two representative TMD MLs (MoS₂ and WS₂). To study their electrical properties, we fabricate large arrays of metal/stacked film/metal vertical tunnel devices as shown in Figure 2.3a and b. Here, we choose gold as the electrode metal, forming a tunnel band diagram as schematically illustrated in Figure 2.3c. Using the tunnel device geometry, we can investigate the uniformity and high quality of PVS films accurately over large area, because tunneling is exponentially sensitive

to the barrier properties including the thickness, band structure, doping, and defects.

Figure 2.3d shows the representative current density versus bias (J - V) curves measured from N_L -layer MoS₂ films ($N_L = 3, 5, 7$). All three J - V curves show similar non-Ohmic behavior, with the current increasing superlinearly with increasing bias. In addition, the magnitude of J strongly depends on N_L , decreasing approximately ten-

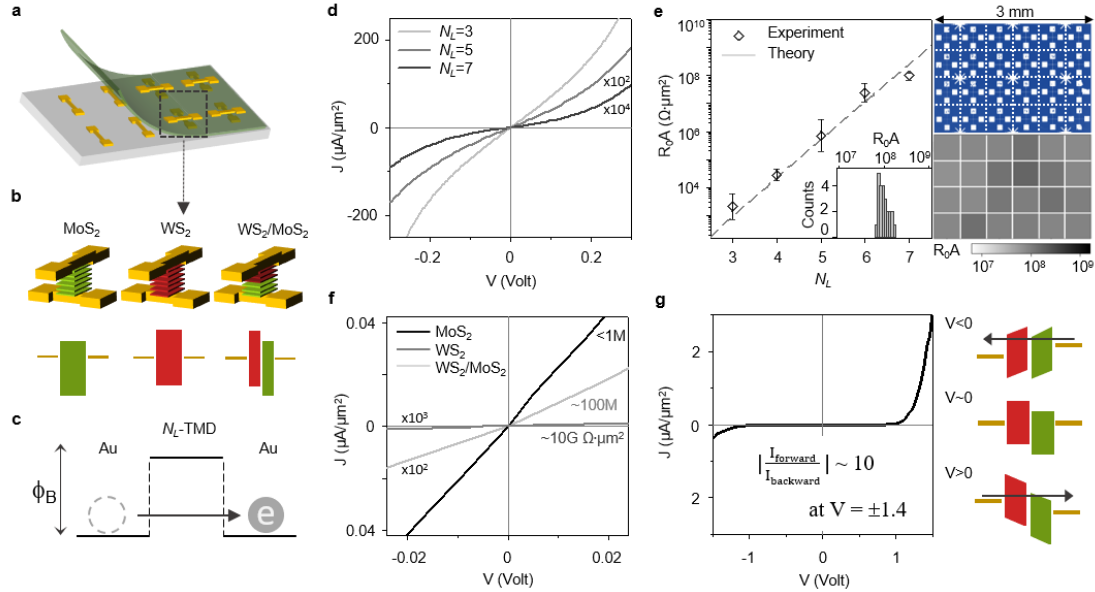


Figure 2.3. Band Engineering of Tunnel Junctions. **a**, a schematic of our device geometry, where a stacked film is sandwiched between top and bottom electrodes. **b**, schematics of devices with different film compositions (top) and their corresponding band profiles (bottom). **c**, a schematic of the general band profile in our devices. **d**, J - V characteristics measured from three Au/ N_L -MoS₂/Au devices with $N_L = 3, 5, 7$. The curves are multiplied by 10^2 ($N_L = 5$) and 10^4 ($N_L = 7$). **e**, (left) zero-bias tunnel resistance-area product measured as a function of N_L . Each data point is an average measured from ten devices; the dashed line is calculated using a tunnel model with a single parameter $\phi_B = 0.5\text{eV}$; (right top) optical image of an array of 24 tunnel devices made with 7L-MoS₂ over a $2 \times 3 \text{ mm}^2$ area; (right bottom) spatial map and (inset) histogram of tunnel resistance of the 24 devices shown in the optical image. **f**, J - V curves near zero bias measured from MoS₂, WS₂ and WS₂/MoS₂ devices, all with $N_L=6$. The curves for WS₂/MoS₂ and WS₂ are multiplied by 10^2 and 10^3 , respectively. **g**, (left) J - V curve of the heterostructure WS₂/MoS₂ device in the large bias regime, where WS₂ side is grounded. It shows a diode behavior with the forward bias current ~ 10 times larger than reverse bias current at 1.4 volts. (right) the corresponding band diagrams under large reverse bias ($V < 0$), zero-bias ($V \sim 0$), and large forward bias ($V > 0$), which have different effective electron tunnel length. Arrows indicate the direction of electron tunneling.

fold with each additional layer. Figure 2.3e (left panel) further plots the average zero-bias resistance-area product (R_0A ; average from ten devices) as a function of N_L , which confirms the same exponential N_L dependence. This exponential dependence and the superlinear J-V curves strongly suggest that the main transport mechanism in our devices is electron tunneling as schematically shown in Figure 2.3c, which is the same mechanism observed from similar devices made with exfoliated hexagonal boron nitride flakes²³. Furthermore, our experimental data quantitatively match the theoretical zero-bias resistance, which is calculated based on a tunnel model²⁴ using the barrier height ϕ_B as the single fitting parameter (Figure 2.3e dash line, plotted with $\phi_B = 0.5$ eV).

The agreement between our experimental data and the theoretical model indicates that our MoS₂ films have a well-controlled N_L and band energy (*i.e.* doping level) uniform across the entire films without structural inhomogeneities that would strongly affect the tunnel current (*e.g.* cracks, wrinkles, and trapped impurities). This is further supported by the spatial map of R_0A values measured from an array of twenty-four $7L$ -MoS₂ tunnel devices over a 2×3 mm² area (Figure 3e, right panel). It shows a 100% device yield with a uniform tunnel resistance. The tunnel resistance histogram of these measurements (Figure 2.3e, inset) further shows a single narrow peak with a standard deviation that corresponds to a thickness variation of only 0.1 layers (*i.e.*, ~ 70 pm variation; see supplementary notes). Similarly, for larger N_L , the control over N_L and spatial uniformity is demonstrated using capacitance measurements (Figure A2.7a). The average capacitance values measured from N_L -layer MoS₂ capacitors (N_L up to 11) closely follow the $1/N_L$ dependence expected from a parallel plate capacitor with only a small variation.

The electrical properties of our stacked films are also composition-sensitive. As schematically depicted in Figure 2.3b for three example devices of ($6L$ -)MoS₂,

(6L-)WS₂ and WS₂(3L)/MoS₂(3L), varying the composition drastically modified the tunnel band profiles of the devices. Figure 2.3f presents the J-V curves of these devices near zero bias, showing up to ~ 10,000-fold increase in resistance when the composition of the film is changed from MoS₂ (< 1 MΩ·μm²) to WS₂ (~ 10 GΩ·μm²). In addition, an intermediate value of ~ 100 MΩ·μm² is observed from the WS₂/MoS₂ heterostructure device. The different band alignments of MoS₂ versus WS₂ (Figure 2.3b, bottom) explains this large tuning range. Even though MoS₂ and WS₂ have similar bandgap energies, E_F of gold is closer to the center of the WS₂ bandgap²⁵, leading to a higher tunnel barrier and thus larger resistance for the WS₂ device. Similarly, the effective barrier height in the heterostructure WS₂/MoS₂ device is approximately the average of those of MoS₂ and WS₂, explaining the intermediate tunnel resistance value²⁴. Moreover, the heterostructure WS₂/MoS₂ device shows an asymmetric, diode-like J-V curve at larger biases (Figure 2.3g), with the forward bias current ~ 10 times larger than reverse bias current at 1.4 volts, in contrast to the symmetric curves of MoS₂ and WS₂ devices (Figure A2.7b). This is similar to the characteristic behavior of the metal-insulator-insulator-metal (MIIM) tunnel diode recently reported²⁶, where the effective tunnel distance changes depending on the bias direction due to the barrier height offset at the insulator-insulator interface. (see right panel of Figure 2.3g).

2.5. Freestanding Ultrathin Film for Optical and Mechanical Applications

Because of the van der Waals nature of 2D materials, they are highly detachable and transferable, making them compatible with various environments and processing. However, this advantage of 2D materials can only be fully utilized when the sample is large and high quality, which we have achieved here with the PVS process. Hence, many applications of 2D materials become practical. For instance, the

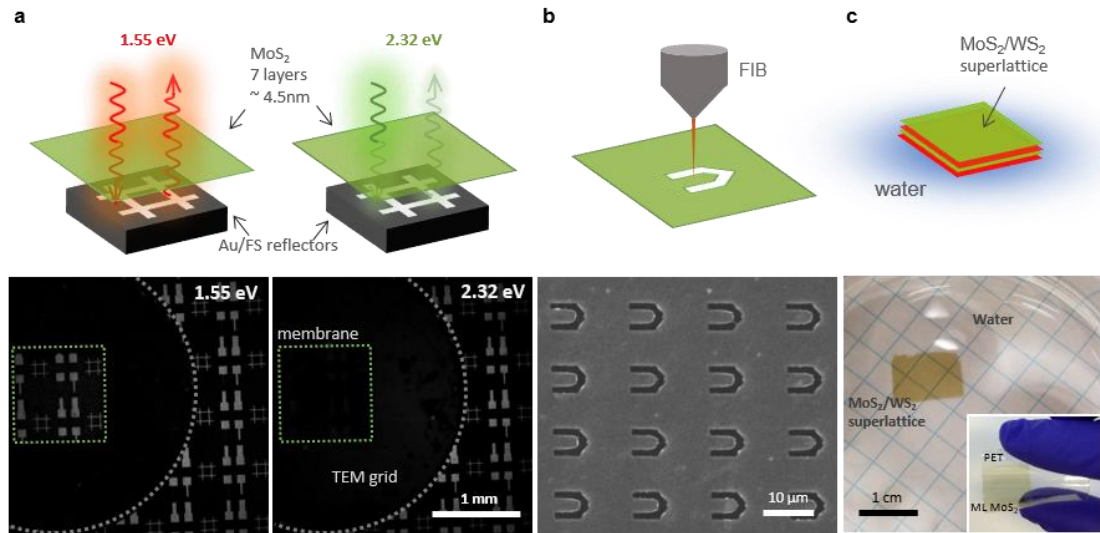


Figure 2.4 Large-scale free standing TMD films. **a**, top: schematics of a $7L$ - MoS_2 film as an ultrathin optical window with color-tunable transparency; bottom: optical reflection images of patterned gold reflectors at two different photon energies taken with the window (inside the green dotted square) suspended $\sim 200 \mu\text{m}$ above the substrate. The window is transparent at 1.55eV (below E_g , left image), but is opaque at 2.32eV (above E_g , right image), as compared to the window-free area (outside the circle). **b**, bottom: SEM image of cantilever-shaped structures generated within a $7L$ - MoS_2 membrane. They are made using FIB milling (shown in the top schematic). **c**, a $4L$ - MoS_2/WS_2 superlattice floating on water surface with no additional support (schematic on top). Inset: a photo of a $1''$ -scale ML MoS_2 film transferred onto a plastic (PET) substrate from water.

films can be suspended to produce ultrathin windows, patterned to generate freestanding structures, or transferred to form unconventional interfaces, as we demonstrate below.

Figure 2.4a first demonstrates the use of films as an optical window with color-tunable transparency. An array of patterned gold reflectors is imaged through the freestanding $7L$ - MoS_2 film ($1 \times 1 \text{ mm}^2$, shown in Figure 2.1c) at two different photon energies, each below and above E_g of MoS_2 ($\sim 1.86 \text{ eV}$). At 1.55 eV , the reflector array is clearly imaged with the MoS_2 window, showing no significant intensity difference compared to the window-free area. At 2.32 eV , however, the features under the window are barely visible as the MoS_2 film becomes opaque due to its strong absorption at this wavelength. Another example of applications is the fabrication of

freestanding structures within our films. Figure 2.4b (bottom) shows an SEM image of an array of cantilever-shaped structures, patterned using a focused ion beam (FIB) milling. This process allows us to pattern ultrathin semiconductor structures with an arbitrary shape, such as cantilevers or holes, which could lead to a new class of micro- and nano-electromechanical systems²⁷ and nanoporous membranes²⁸. Finally, Figure 2.4c shows a large-scale $4L$ -Mo/W/Mo/WS₂ superlattice film floating on the water surface, generating a semiconductor/water interface. It is delaminated from a substrate by simply dipping it into water²⁹ with no polymer support, which provides another way of releasing the stacked films onto surfaces with different thermal/chemical nature, such as plastic substrates (inset photo).

2.6. Summary

Our PVS process offers a powerful platform for systematically generating previously unavailable large-scale heterostructures and devices whose properties are designed with atomic scale precision. For example, its application to emerging layered materials, including monolayer superconductors¹⁶ and ferromagnets¹⁷, would produce novel interfaces and superlattices where superconductivity and magnetic orders coexist, with the coupling between them being tuned layer-by-layer. The integration of the large-scale tunnel barriers demonstrated in this work with conventional superconductors and ferromagnets could also lead to the batch fabrication of novel Josephson junction arrays and spintronic devices, which we will explore in Chapter 4. Furthermore, it could be used for vertical manufacturing of hybrid materials and devices, where non-layered materials, such as organic films and self-assembled nanostructures, are stacked vertically, layer by layer, along with the two-dimensional materials. These potentials will accelerate the discovery of novel materials and the large-scale development of ultrathin multifunctional integrated circuitry.

2.7. Appendix

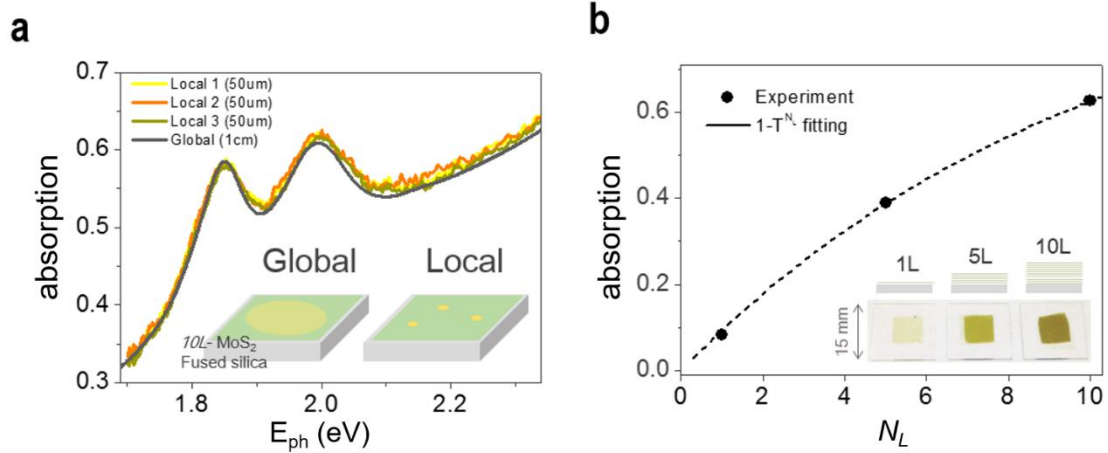


Figure A2.1 Optical absorption spectra of N_L - MoS_2 films. **a**, spectra of $10L$ - MoS_2 measured at three random locations (local 1- 3) with spot size $\sim 50 \mu\text{m}$, compared to spectrum using $\sim 1 \text{ cm}$ spot size (labeled as ‘global’). All spectra are similar, indicating the film has spatially uniform properties. Inset: schematics of the sample and the measurements. (spots not drawn to scale.) **b**, absorption measured at 532 nm as a function of N_L using a 1cm spot size. The trend follows the expected layer dependent absorption $1-T^{N_L}$ with $T = 0.91$, close to the value for ML MoS_2 . Inset: Schematics and photos of the measured films, $N_L=1, 5, 10$.

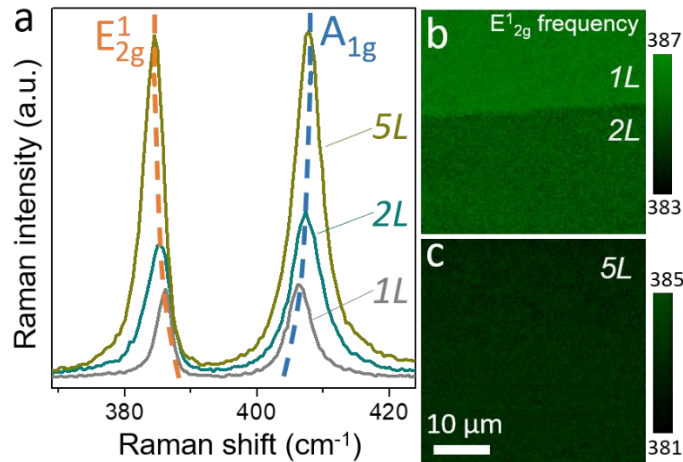


Figure A2.2 Uniform Raman properties of PVS-stacked MoS_2 films. **a**, Raman spectra taken from $1L$ -, $2L$ - and $5L$ - MoS_2 . Dashed lines track the trajectory of peak frequency as a function of N_L . **b**, Raman frequency mapping of E_{2g}^1 peak across $1L$ - and $2L$ - MoS_2 films. **c**, Raman frequency mapping of E_{2g}^1 peak at $5L$ - MoS_2 . All regions show uniform and consistent Raman properties.

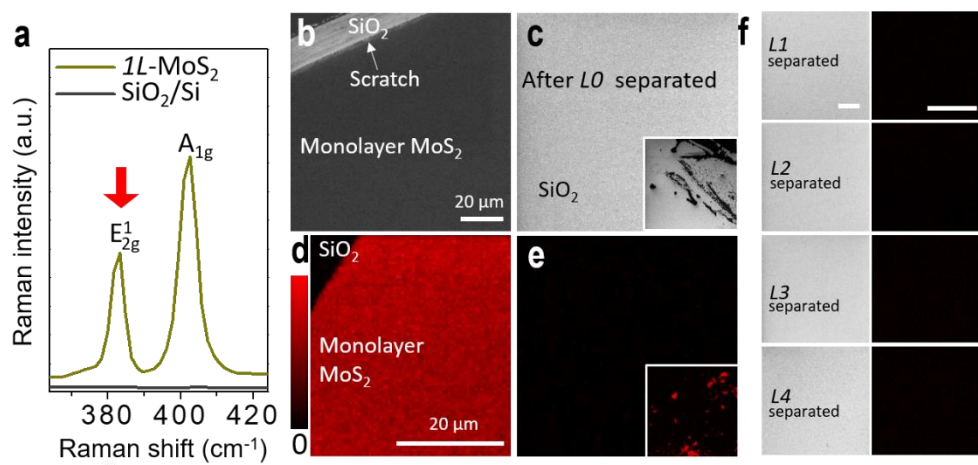


Figure A2.3 High yield of mechanical peeling. **a**, Raman spectra taken on SiO₂/Si substrates with (dark yellow) and without (grey) as-grown 1L-MoS₂. The E_{2g}¹ peak (indicated by a red arrow) is used for Raman mapping below. **b**, **c**, SEM images of 1L-MoS₂ and a substrate after the MoS₂ is successfully separated. Left-top scratch in **b** is made intentionally to expose SiO₂ for contrast. Inset of **c**: an example of failed peeling when low quality MoS₂ is used. **d**, **e**, Raman peak area mapping around the E_{2g}¹ peak frequency in correspondence to the SEM in **b** and **c**; inset of **e** for failed peeling. **f**, SEM (left column), Raman E_{2g}¹ peak area mapping (middle) and Raman spectra from five random locations (right column) taken on a series of substrates after additional peeling steps (generating L1, L2, L3, and L4). No MoS₂ residues are observed in any of the images, indicating a nearly perfect peeling yield regardless of the number of repeated peeling and stacking. Scale bars: 20 μm.

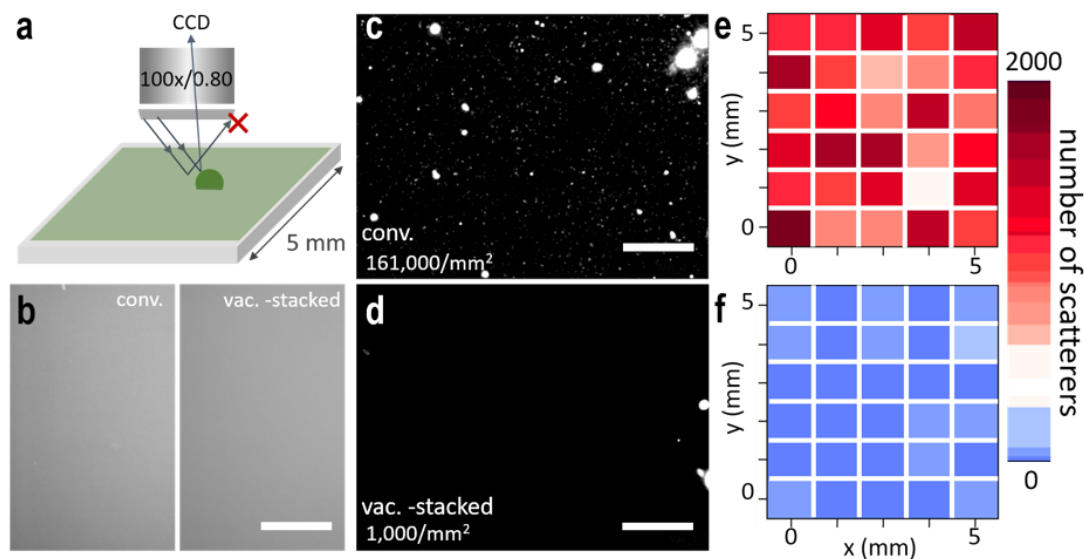


Figure A2.4 Dark-field optical microscope imaging. The $2L$ - MoS_2 are generated by conventional dry transfer (c and e) and PVS (d and f) methods. **a**, a schematic of the experimental set-up. **b**, bright field microscope images. **c** and **d**, representative dark-field images of each sample. **e** and **f**, scatterer number maps generated using thirty DF images taken over $5 \times 5 \text{ mm}^2$ sample area. Scale bars: $20 \mu\text{m}$.

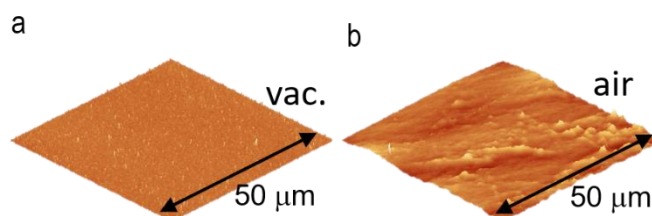


Figure A2.5 Additional $50 \times 50 \mu\text{m}^2$ AFM images. Data is taken from the bottom side of $2L$ - MoS_2 films stacked **a**, in vacuum and **b**, in air. The height scale is $\pm 25 \text{ nm}$.

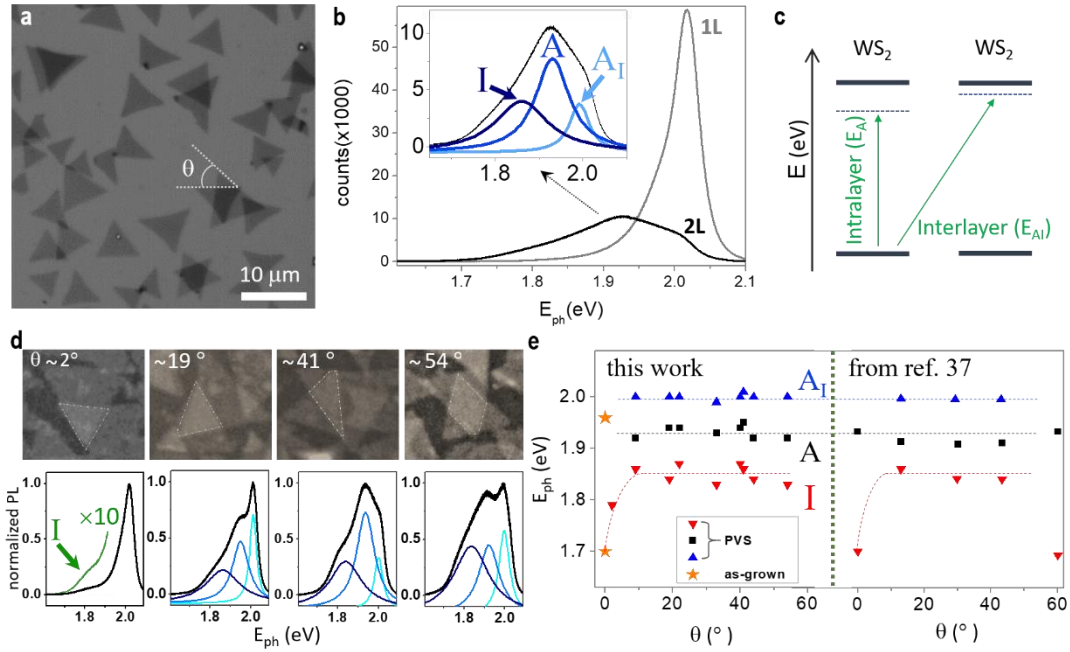


Figure A2.6 Interlayer coupling in PVS-stacked bilayer WS_2 . **a**, optical image of the sample. We approximate the twist angle using the edge orientation of each layer. **b**, PL spectra of $1L$ - and $2L$ - WS_2 . Inset: zoom-in of the spectrum for $2L$ - WS_2 . The peak can be fitted by three peaks: indirect transition peak I, direct transition peak of intralayer exciton (A) and direct transition of interlayer exciton peak (A_I). **c**, schematics of the transitions for intralayer and interlayer A excitons of WS_2 . **d**, optical images and PL spectra of $2L$ - WS_2 regions with different twist angles. **e**, angle-dependence of (left) PVS-stacked WS_2 compared to (right) those reported in ref. 37.

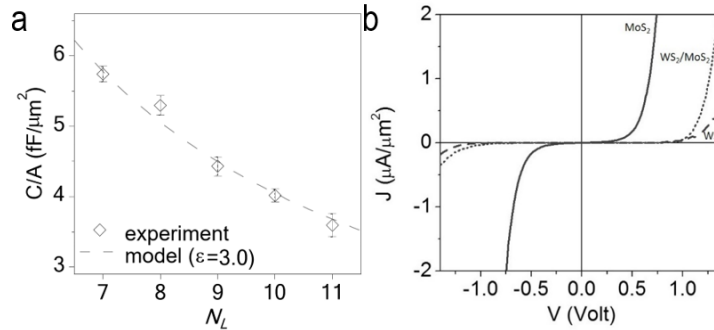


Figure A2.7 Additional electrical characterization. **a**, Capacitance per unit area versus N_L . Each data point is the average of ten devices. The dashed line is calculated for a parallel plate capacitor with a dielectric constant $\epsilon = 3.0$. The error bars are the standard deviation. **b**, J-V curves of $6L$ - MoS_2 , $6L$ - WS_2 and $\text{WS}_2(3L)/\text{MoS}_2(3L)$ devices at large bias regimes. For the MoS_2 device, the J-V curve is symmetric for the entire V range. For WS_2 , it is generally symmetric, with only a small bias-dependence asymmetry ($|I(\text{forward})/I(\text{reverse})| < 2$ at $V = \pm 1.4$). In contrast, the WS_2/MoS_2 device displays a much larger asymmetry ratio $|I(\text{forward})/I(\text{reverse})| > 10$ at $V = \pm 1.4$.

2.8. References

1. Sedra, A. S., Smith, K. C. Microelectronic circuits (Oxford Univ. Press, Oxford, 6th ed., 2009).
2. Nakamura, S. *et al.* InGaN-based multi-quantum-well-structure laser diodes. *Japanese J. Appl. Physics, Lett.* **35**, L74-L76 (1996).
3. Faist, J. *et al.* Quantum cascade laser. *Science* **264**, 553 (1994).
4. Geim, A. K., Grigorieva, I. V. Van der Waals heterostructures. *Nature* **499**, 419 (2013).
5. Liu, Y. *et al.* Van der Waals heterostructures and devices. *Nat. Rev. Mater.* **1**, 16042 (2016).
6. Novoselov, K. S., Mishchenko, A., Carvalho, A., Castro Neto, A. H. 2D materials and van der Waals heterostructures. *Science* **353**, 461 (2016).
7. Wang, L. *et al.* One-dimensional electrical contact to a two-dimensional material. *Science* **342**, 614 (2013).
8. Xu, W. *et al.* Correlated fluorescence blinking in two-dimensional semiconductor heterostructures. *Nature* **541**, 62 (2016)
9. Hunt, B. *et al.* Massive Dirac fermions and Hofstadter butterfly in a van der Waals heterostructure. *Science* **340**, 1427 (2013).
10. Rivera, P. *et al.* Valley-polarized exciton dynamics in a 2D semiconductor heterostructure. *Science* **351**, 688 (2016).
11. Kim, C. -J. *et al.* Chiral atomically thin films. *Nat. Nanotech.* **11**, 520 (2016).
12. Haigh, S. J. *et al.* Cross-sectional imaging of individual layers and buried interfaces of graphene-based heterostructures and superlattices. *Nat. Mater.* **11**, 764 (2012).
13. Lee, Y. G. *et al.* Quantitative analysis of hysteretic reactions at the interface of graphene and SiO₂ using the short pulse I-V method. *Carbon* **60**, 453 (2013).
14. Kretinin, A. V. *et al.* Electronic properties of graphene encapsulated with different two-dimensional atomic crystals. *Nano Lett.* **14**, 3270 (2014).
15. Chiu, M. -H. *et al.* Spectroscopic signature for interlayer coupling in MoS₂-WSe₂ van der Waals stacking. *ACS Nano* **8**, 9649 (2014)
16. Kang, K. *et al.* High-mobility three-atom-thick semiconducting films with wafer-scale homogeneity. *Nature* **520**, 656 (2015).

17. Liu, K. *et al.* Evolution of interlayer coupling in twisted molybdenum disulfide bilayers. *Nat. Commun.* **5**, 4966 (2014).
18. Kim, D. H. *et al.* Stretchable and foldable silicon integrated circuits. *Science* **320**, 507 (2008).
19. Jang, H. *et al.* Quantum confinement effects in transferrable silicon nanomembranes and their applications on unusual substrates. *Nano Lett.* **13**, 5600 (2013).
20. Li, B. *et al.* Scalable transfer of suspended two-dimensional single crystals. *Nano Lett.* **15**, 5089 (2015)
21. Yun, W. S., Han, S. W., Hong, S. C., Kim, I. G., Lee, J. D. Thickness and strain effects on electronic structures of transition metal dichalcogenides: 2H- MX₂ semiconductors (M = Mo, W; X = S, Se, Te). *Phys. Rev. B* **85**, 033305 (2012).
22. Zheng, S. *et al.* Coupling and interlayer exciton in twist-stacked WS₂ bilayers. *Adv. Opt. Mat.* **3**, 1600 (2015).
23. Britnell, L. *et al.* Electron tunneling through ultrathin boron nitride crystalline barriers. *Nano Lett.* **12**, 1707 (2012).
24. Simmons, J. G. Generalized formula for the electric tunnel effect between similar electrodes separated by a thin insulating film. *J. Appl. Phys.* **34**, 1793 (1963).
25. Kang, J. S., Tongay, J., Zhou, Li, J., Wu, J., Band offsets and heterostructures of two-dimensional semiconductors. *Appl. Phys. Lett.* **102**, 012111 (2013).
26. Maraghechi, P., Foroughi-Abari, A., Cadien, K., Elezzabi, A. Y. Enhanced rectifying response from metal-insulator-insulator-metal junctions. *Appl. Phys. Lett.* **99**, 1 (2011).
27. Baek, S. H. *et al.* Giant piezoelectricity on Si for hyperactive MEMS. *Science* **334**, 958 (2011).
28. Feng, J. *et al.* Single-layer MoS₂ nanopores as nanopower generators. *Nature* **536**, 197 (2016).
29. Gurarlan, A. *et al.* Surface-energy-assisted perfect transfer of centimeter-scale monolayer and few-layer MoS₂ films onto arbitrary substrates. *ACS Nano* **8**, 11522 (2014).

CHAPTER THREE

Quantum Confined Stark Effect in Twisted Bilayer Graphene

3.1. Introduction

Two-dimensional (2D) materials, such as graphene and transition metal dichalcogenides, generally have electrical and optical properties that are sensitive to the environment owing to their atomically-thin nature.^{1,2} Such high tunability of 2D materials allow their properties to be simply controlled through electrostatic gating, and therefore makes them promising candidates for many applications where electrically tunable properties are critical. Important examples are 2D material-based transistors²⁻⁶, tunable lasers⁷, photodetectors^{8,9}, and optical modulators^{10,11}. Among 2D materials, twisted bilayer graphene (tBLG) has particularly interesting electrical and optical properties. In tBLG, the angle of the crystal orientation between the constitutional layers are finite. This twist angle induces the angle-dependent van Hove singularities (VHSs) in its band structure at the intersections of the two Dirac cones from each layer, where the intra-layer states hybridize into inter-layer states (Figure 1a, inset). This allows additional strong transitions between VHSs and give rise to the extra angle-dependent interlayer optical resonance peaks in the optical absorption spectrum of tBLG in comparison to that of Bernal-stacked BLG (shown in Figure 3.1a).¹²⁻¹⁵ Previous work has reported many unique properties of this interlayer optical resonance. For example, the interlayer optical resonance transitions exhibit excitonic nature, where the excitons are first identified as resonant excitons rather than the

¹Kan-Heng Lee, Dr. Robin Havener and Prof. Jiwoong Park conceived the idea. Kan-Heng Lee and Dr. Robin Havener developed the device structures and carried out the optical and electrical characterizations. Kan-Heng Lee wrote the manuscript with Prof. Jiwoong Park.

common bound excitons.¹⁶ Later theory predicts that additional bound excitons are also generated along with the resonant excitons in tBLG, but are not accessible by the one-photon measurement previously used.¹⁷ This is experimentally confirmed by the two-photon excitation measurement on tBLG.¹⁸ More recent work shows that the interlayer optical resonance transition also shows strong circular dichroism depending on the handedness of the rotation between the layers of tBLG.¹⁹ However, despite all the intensive studies on the interlayer optical response excitons of tBLG, its optical properties in response to the electrical gating has not been fully characterized and

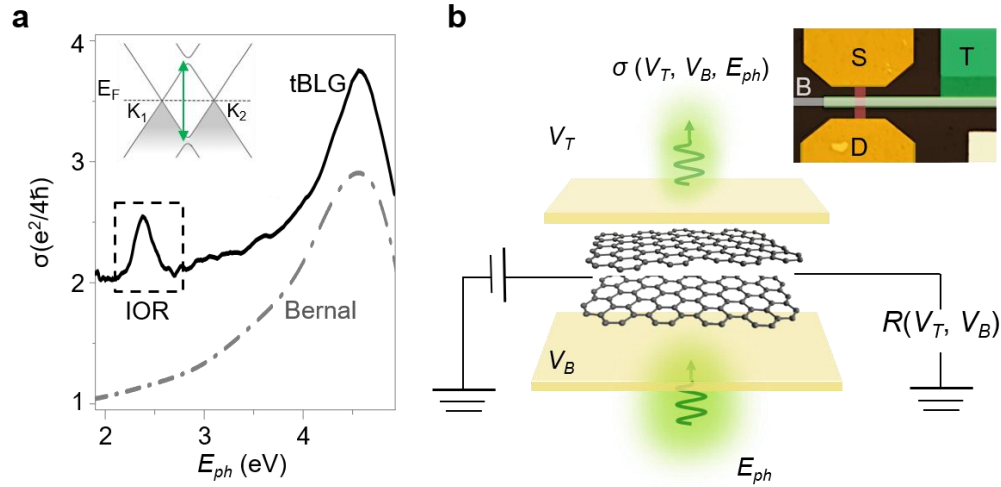


Figure 3.1 Experiment set-up. **a**, the optical conductivity (σ) spectrum of tBLG with twist angle of 13.6° (solid) and Bernal-stacked BLG (dashed). The dashed square enclosed the signature interlayer optical resonance (IOR) peak of tBLG. Inset: the band structure of tBLG. The dashed line shows the Fermi level E_F of undoped tBLG, K_1 , K_2 are the Dirac points from each constitutional layer, and the green arrow indicates the transition corresponding to the interlayer optical resonance peak. **b**, Schematics of the experiment set-up. Gate voltages are separately addressed by top (V_T) and bottom gate (V_B). A bias voltage is applied to tBLG and the resistance is measured as a function of (V_T , V_B). White light is shined from the bottom-gate and the full optical transmission spectrum is collected after top gate as a function of V_T , V_B and photon energy E_{ph} . Inset: false color optical image of the device. S, D, B, T represents source, drain, bottom and top gate electrode, respectively. The red stripe is the tBLG channel, where the channel length is $30 \mu\text{m}$.

understood so far.

The electro-optical properties in 2D materials have been intensively studied previously²⁰⁻²³. However, the two components of the electrical gating— *i.e.*, the electric field and the doping—are usually convoluted or only theoretically distinguished by estimate based on simulations. Moreover, since unwanted exotic doping can easily happen during the fabrication or measurement of 2D materials, characterizations could potentially have significant inaccuracy if the doping and electric field on the sample is not monitored during measurement. Hence, a method that allows individual control of the electric field and the doping, as well as a measurement of the exact magnitude of these variables, are essential to quantitatively understand the optical response of 2D materials as a function of electrical gating. In this work, we developed such a characterization method that enables simultaneous measurements of the electric field and doping during the optical measurement, and use the method to understand the electro-optical properties of tBLG.

3.2. Method of simultaneous electrical and optical characterizations

Figure 3.1b schematically summarizes our experiment set-up. The tBLG is embedded in a dual gate transistor device as the channel material between source and drain electrodes. The gate electrodes are fabricated using thin gold metal to allow transmission of the light at the measuring wavelengths. The optical microscope image of the device is displayed in the inset. With this device geometry, we simultaneously measured tBLG's resistance (R) and full optical transmission (σ) spectrum around the interlayer optical response peak for each top (V_T) and bottom (V_B) gate voltage. As we

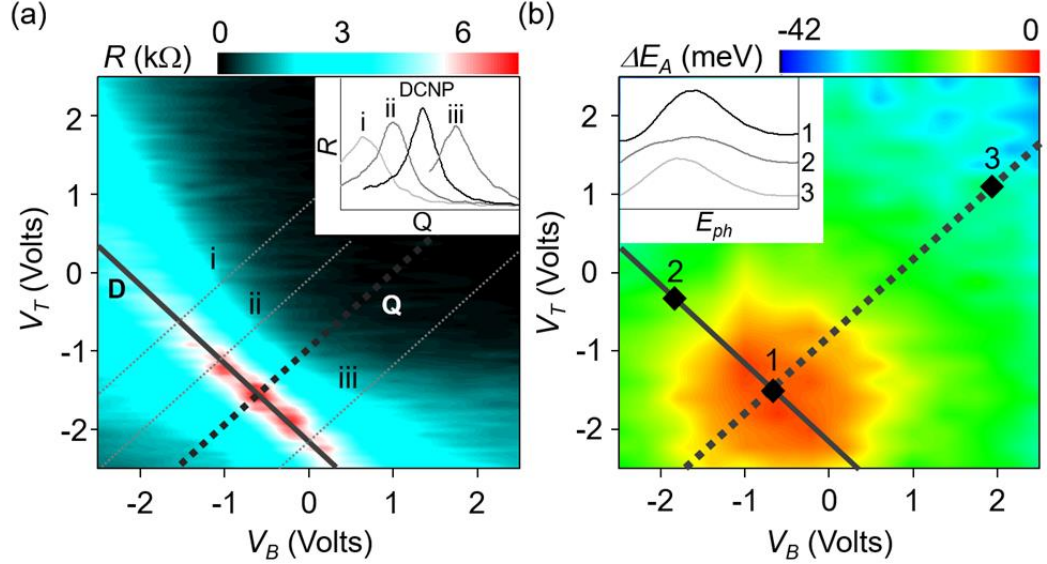


Figure 3.2 Simultaneous electrical and optical measurements. **a**, color plot of the resistance R as a function of V_T and V_B . Along the D-line (the solid line), there is only electric field but no overall doping charges; along the Q-line (the dotted thick line), there is doping but no electric field. Along (i)-(iii), both the doping and the electric field are in present. Inset: resistance profiles along (i), (ii), Q and (iii). The maximum R along Q is the maximum of all the curves, indicating it is the DCNP of tBLG. (see main text.) **b**, color plot of the IOR peak energy shift ΔE_A , in relative to the maximum peak energy, as a function of V_T , V_B . The solid and dashed lines are drawn based on the D- and Q-lines in **a**. Inset: The σ -spectra of IOR at 1 (DCNP), 2 (high D) and 3 (high Q). It clearly shows that both D and Q significantly changes the line-shape of IOR. The y-axis of the inset plot is σ of tBLG subtracted by σ of Bernal BLG.

will explain later, R as a function of V_T and V_B can be used to extract the exact electric field (D) and doping (Q) experienced by the tBLG under each gating condition. Based on this, the simultaneously measured σ -spectrum can be precisely determined as a function of D , Q and photon energy E_{ph} . In our experiment, the tBLG's are produced with two monolayer graphene films that are grown on the same Cu (111) grain and then cut in half, hence have the same lattice orientation as described in Ref²⁴). These layers are then stacked together with a designed twist angle by rotating one of the graphene layers with that angle relative to the other. This method is also previously reported¹⁹ (see also Figure A3.1 in the appendix for details). Five devices are

fabricated with tBLG having twist angles ranging from 9.9° to 13.6° , confirmed by the peak energy (E_A) of the interlayer optical response. The data shown below are representative data from two of the devices with $\theta=10.7^\circ$ (for all except Figure. 3a and 4a) and $\theta=12.1^\circ$ (Figure. 3a and 4a). All five devices show similar results.

Figure 3.2 shows the result of the simultaneously measured electrical and optical properties of the tBLG as a function of the gating. Figure 2a first displays the color plot of $R(V_T, V_B)$, from which we can extract the exact D and Q applied onto the tBLG using the graphene parallel plates capacitor model described in ref. ²⁵. Briefly, the high resistance line (solid line, marked as D) indicates that the tBLG is in an undoped state $Q = 0$, leaving D as the main variable. Lines perpendicular to the D-line thus have fixed D 's and leave Q as the main variable. The inset of Figure 2a shows the resistance profile of these lines (i-iii and Q). Based on the model, the maximum of the peak resistances of these lines occurs exclusively at the double charge neutrality point (DCNP), where both D and Q vanish. This gives us the ability to experimentally calibrate the zero of both D and Q applied on tBLG, which are ignored or assumed in previous studies. With this, we can also define the line perpendicular to the D-line and passing through the DCNP as the Q-line, where we can exclude the effect of D . We note here that, as clearly shown in Figure 3.2a, the location of the DCNPs are significantly away from the zero gate voltage in most of the devices. Moreover, the amount the DCNPs shift varies from device to device depending on the growth and fabrication batches. Therefore, this additional step of using the well-understood tBLG electrical behavior allows us to measure the real electrical gating applied to the sample, regardless of exotic effects.

Figure 3.2b further shows the interlayer optical response peak energy shift (denoted as ΔE_A) in relative to the maximum value, which is simultaneously measured with Figure 2a. The peak energies E_A 's are extracted by Gaussian fitting each optical absorption spectra around the interlayer optical response peak of tBLG at different values of V_T and V_B . The D- and Q- lines, on the other hand, are drawn according to the results discussed in Figure 3.2a. Our data clearly shows that the maximum E_A (i.e. $\Delta E_A=0$) overlaps with the DCNP point. Indeed, as we will discuss below, this overlapping is consistent with our theoretical calculation using density functional theory (DFT). Moreover, Figure A3.2 in the appendix shows that the minimum peak width and maximum peak height also occur at the DCNP, which as well matches the DFT calculation. Based on these results, our data in Figure 3.2 proves that our simultaneous electrical and optical measurements are consistent with each other at each gating condition. This offers us the capability to individually and quantitatively characterize the optical response of tBLG to the electric field and the doping. For instance, the inset of Figure 3.2b shows the σ -spectra of interlayer optical response at point 1 (DCNP), 2 ($D \neq 0$, $Q=0$) and 3 ($D=0$, $Q \neq 0$) marked in Figure 2b. Clearly, D and Q both significantly alters the line-shape of the interlayer optical response peak, but the changes of the line-shape are different. In the following, we further utilize our method to study the underlying mechanism of these changes in tBLG, starting with the case when D is applied to the tBLG while $Q = 0$.

3.3. *Quantum confined Stack effect in twisted bilayer graphene*

Figure 3.3a first shows the representative σ -spectra of the interlayer optical

response peak at different D 's. We observed three major changes in all our devices in response to the increasing D : the E_A shifts to lower energies, the widths of the IOR peak are broadened, and the maximum peak heights decrease. In Figure 3b, we further plot the ΔE_A as a function of the electric field determined in Figure 3.2. We found that, first, ΔE_A redshifts monotonically on both sides of the DCNP. Second, the redshift varies non-linearly as a function of D near the DCNP. The order of the non-linearity is further determined in Figure A3.3 in the appendix to be closed to 2, indicating a quadratic dependence of ΔE_A upon the applied electric field D .

Here, we ascribe the quadratic redshift to be the result of the DC quantum-confined Stark effect (QCSE) of the resonant excitons of tBLG. DC QCSE describes the effect when excitons are polarized and elongated under a DC electric field along the quantum-confined direction.²⁶⁻²⁸ This results in redshifts that can be described by a simple quadratic function of D ,

$$\Delta E_A = p \times D + \alpha \times D^2 \dots\dots (1),$$

where p , α are the permanent dipole moment and the polarizability of the exciton along the direction of D . In Figure 3.3b, the solid line represents the fitting of eq. 1 to the experiment result, with the p , α as the fitting parameters. This fitting is in good agreement with our experiment up to $D=50 \times 10^5$ V/cm, and shows that the α of the interlayer optical response exciton is $122 \pm 5 \text{ \AA}^3$. The DC QCSE is also recently observed for the bound excitons in mono- and few- layer MoS₂ using a photo-capacitor device.²³ In the same report, the α of MoS₂ is estimated using finite-element simulations to be roughly 180 \AA^3 regardless of the number of layers, which is comparable to our result here for tBLG.

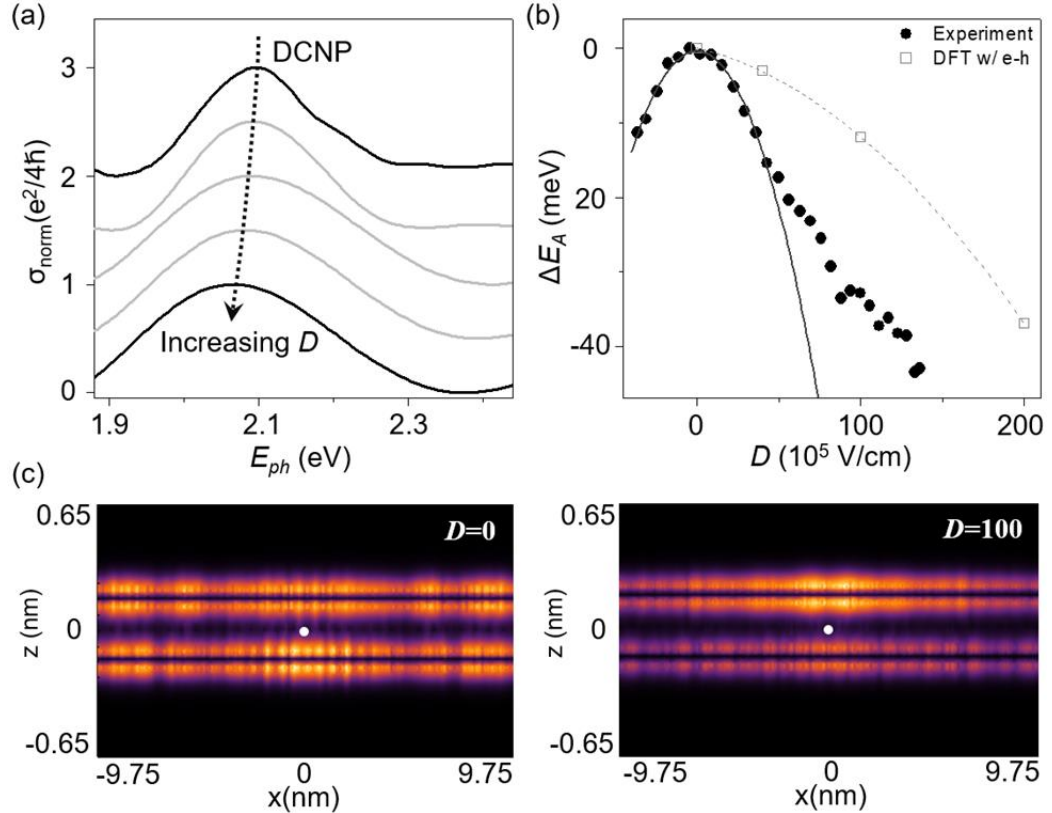


Figure 3.3 Quantum confined Stark effect. **a**, σ -spectra of IOR at different D 's. σ_{norm} indicates that the spectra was subtracted by that of Bernal BLG. It is shown that the IOR peak is redshifted, broadened and decreased in peak height with increasing D . **b**, ΔE_A as a function of D . The solid circles and the empty squares are the experimental data and the theory values from our GW-BSE DFT calculation, respectively. The solid line is the fitting from eq. (1). **c**, Calculated electron spatial distribution of one of the significant states contributed to the IOR at $D=0$ (left) and $100 \cdot 10^5 \text{V/cm}$ (right). D is applied along z -axis from positive to negative. The intensity shows the absolute square of electron's wavefunction integrated out in the y -direction when the hole is fixed at the center (white dots).

The DC QCSE picture is also supported by our DFT calculation including many-body interactions (GW-BSE DFT). The empty squares in Figure 3.3b show the calculated ΔE_A for a tBLG with $\theta=21.8^\circ$, which qualitatively captures the D^2 -dependence of the redshift as we observed in the experiment. In contrast, previous report calculating the electric field dependence of tBLG's interlayer optical response peak using a simple single particle picture (, i.e. when excitons are not considered,) shows a moderate blueshift on D .¹⁵ This confirms that the D^2 -redshift indeed comes

from the excitonic nature of the interlayer optical response, and is the dominant effect for the optical response of tBLG under electric field. In Figure 3.3c, we further plot out the electron spatial distribution of one of the significant energy states of interlayer optical response when D is applied along the out-of-plane direction from positive to negative z -coordinate. The intensity shows the absolute square of electron's wavefunction integrated in the y -direction when the hole is fixed at the middle of the tBLG layers (white dots). It clearly shows that the uniformly distributed excitons at $D=0$ are polarized along the electric field at $D=100$ (10^5V/cm), which is consistent with the picture of DC QCSE. On the other hand, both DC QCSE and single particle model predicts peak broadening and suppression as we observed in Figure 3.3a, and therefore we attribute the changes of the peak widths and heights to be a result of the convolution of both the QCSE and the deformation of the single-particle band structure as schematically illustrated in Figure A3.4 in the appendix.

3.4. Many-body interactions in twisted bilayer graphene

Now we turn to the response of interlayer optical response peak when there is finite doping but no electric field. Figure 3.4a shows the representative spectra of the interlayer optical response at different Q 's. As Q increases, we observed redshifts of E_A , broadening of the peak width, and decrease of the peak maximum. Figure 3.4b further plots the ΔE_A against Q and shows that the redshifts of the interlayer optical response peak energies is now a linear function of Q , in contrast to the quadratic dependence on D . This linear dependence of the redshifts upon doping is independent of the signs of the doping charges, and the slope is extracted to be $(12.6 \pm 0.4) \times 10^{-12}$

(meV cm²/e) from Figure 3.4b.

To understand the effect of doping, we again examine our experimental results against the single particle model and the GW-BSE DFT calculations. In the single particle picture, it is predicted that the changes of the interlayer optical response peak occur when the doping level reaches the VHS energies, causing a suppression of the transitions through Pauli-exclusion principle. Nonetheless, the standard gating geometry we use in the experiment can only shift the Fermi level up to a few hundreds of meV, much less than the VHS energies of $\sim\pm 1$ eV that would result in Pauli-blocking. Therefore, our observations must be understood as many-body effects. Figure 3.4b shows the theoretical results when the many-body effect is considered. The DFT calculation now shows significant redshifts as Q increases as we experimentally observed, even at a doping level much lower than the VHS energies.

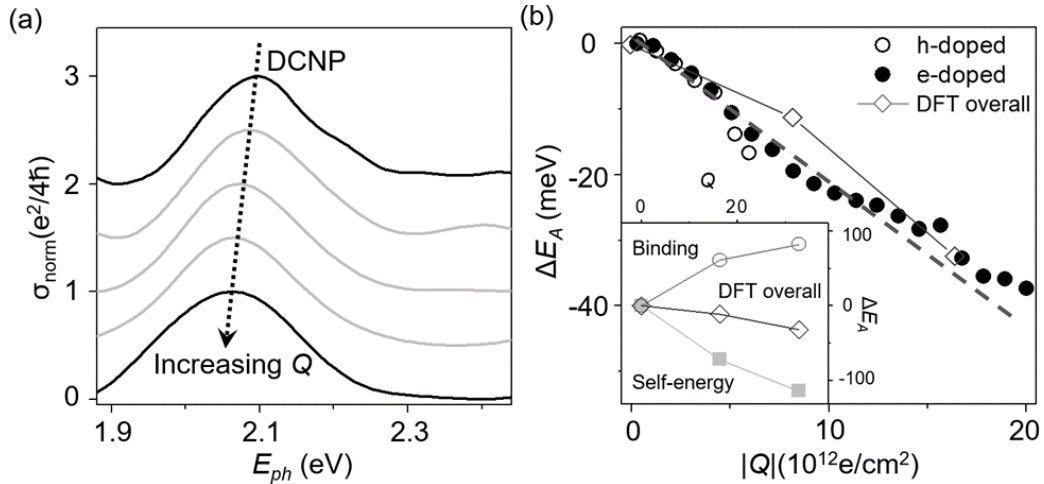


Figure 3.4 Many-body interactions. **a**, σ -spectra of IOR at different Q 's. With increasing Q , the IOR peak shows redshift, broadening and decrease in peak height. **b**, ΔE_A as a function of $|Q|$. Empty and solid circles are experimental data of hole-doping and electron-doping, respectively. Dash line shows the linear fitting. The diamond points are the result from GW-BSE DFT. Inset: the overall redshift (diamond points) due to Q is the sum of the change in quasi-particle self-energy (solid square) and exciton binding energy (circles). In tBLG, the former is slightly larger than the latter, resulting in the redshifts we observed.

Further analysis of the theory indicates that the effect is caused by the screening from the doping charges, and is consisted of two competing components as shown in the inset of Figure 4b: the decrease of the electrons (holes) self-energy (Σ , causing redshifted E_A), and the decrease of exciton binding energy (E_b , causing blueshifts). It is shown that the decrease of the quasi-particle self-energy is slightly higher than the decrease of excitons binding energy, leading to a moderate redshift that is observed in the experiment. In fact, similar many-body effect is responsible for the optical responses upon doping in other 2D materials, such as the M-point transition of monolayer graphene²⁹ and the A-exciton peak of MoS₂³⁰. Indeed, when we compare the slope in Figure. 3.4b of tBLG to that of the monolayer graphene ($\sim 13 \times 10^{-12}$ meV cm²/e), it appears that their response to the doping charges are quantitatively similar, indicating that the effect of charge screening might be the same in both types of graphene systems.

3.5. Summary

The above study of the electro-optical properties of the tBLG has demonstrated the capability of our new characterization method to provide quantitative measurements without the convolutions of the electric field and the doping that are applied to the sample. This is enabled by the simultaneous monitoring of the electric and optical properties of the samples. While here we only demonstrated using tBLG, we expect the method to be universal for many other 2D materials, as long as both the electrical and optical properties of the material respond to the electric field and the doping distinctly. The capability of our method to accurately characterize various 2D

materials under electrostatic gating would potentially enable one to accurately control their properties to generate desired optical functions for future applications such as ultra-thin smart glasses.

3.6. Appendix

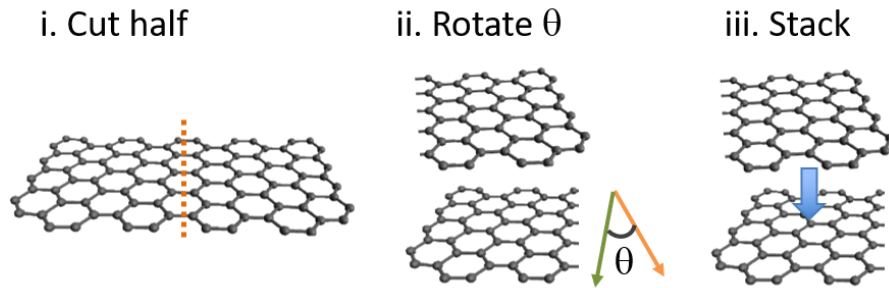


Figure A3.1 Process for making twisted bilayer graphene with a controlled twist angle. A aligned graphene from a single Cu (111) grain is cut in half (each ~ 5 mm), rotate an angle of θ relative to each other, and then stacked together.

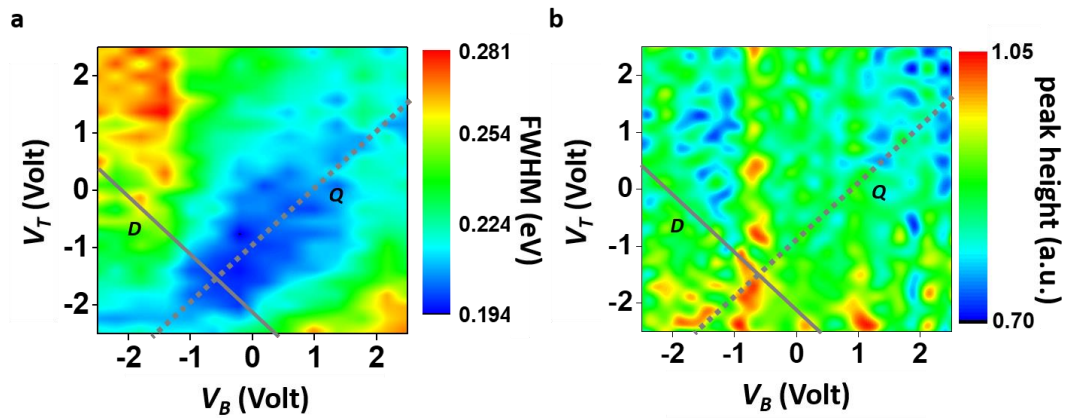


Figure A3.2 Color plots for the interlayer optical resonance peak line shape. **a**, peak width and **b**, peak height.

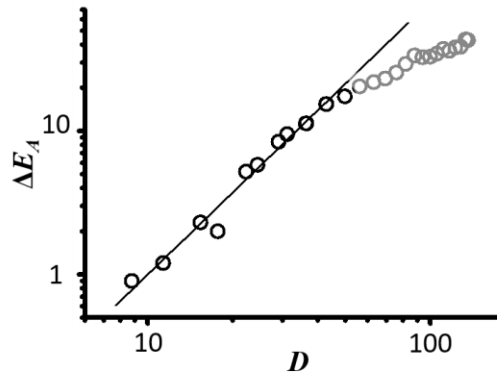


Figure A3.3 Log-log plot of ΔE_A as a function of D . The linear fitting shows that ΔE_A is proportional to D^x , where $x = 1.9 \pm 0.1$.

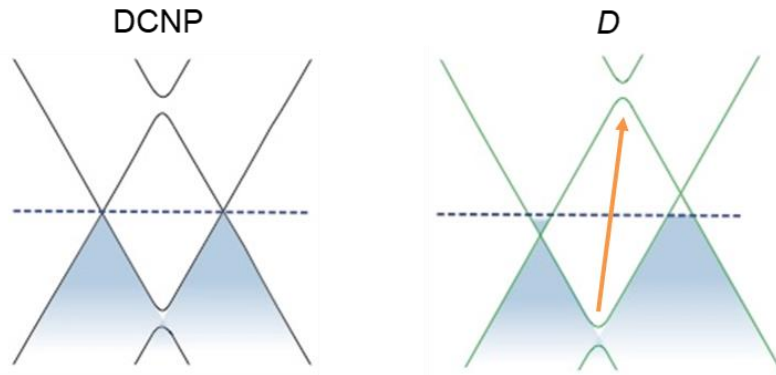


Figure A3.4 Single particle band structure of tBLG under electric field. Note that the transition become indirect in k -space under the electric field.

3.7. References

1. Novoselov, K. S., Jiang, D., Schedin, F., Booth, T. J., Khotkevich, V. V., Morozov, S. V. & Geim, A. K. Two-dimensional atomic crystals. *Proc. Natl. Acad. Sci. U. S. A.* **102**, 10451–10453 (2005).
2. Novoselov, K. S., Geim, A. K., Morozov, S. V., Jiang, D., Zhang, Y., Dubonos, S. V., Grigorieva, I. V. & Firsov, A. A. Electric Field Effect in Atomically Thin Carbon Film. *Science* **306**, 666–669
3. Schwierz, F. Graphene transistors. *Nat. Nanotechnol.* **5**, 487–496 (2010).
4. Radisavljevic, B., Radenovic, A., Brivio, J., Giacometti, V. & Kis, A. Single-layer

- MoS₂ transistors. *Nat. Nanotechnol.* **6**, 147–150 (2011).
5. Kang, K., Xie, S., Huang, L., Han, Y., Huang, P. Y., Mak, K. F., Kim, C.-J., Muller, D. & Park, J. High-mobility three-atom-thick semiconducting films with wafer-scale homogeneity. *Nature* **520**, 656–660 (2015).
 6. Desai, S. B., Madhvapathy, S. R., Sachid, A. B., Llinas, J. P., Wang, Q., Ahn, G. H., Pitner, G., Kim, M. J., Bokor, J., Hu, C., Wong, H.-S. P. & Javey, A. MoS₂ transistors with 1-nanometer gate lengths. *Science* **354**, 99–102 (2016).
 7. Wu, S., Buckley, S., Schaibley, J. R., Feng, L., Yan, J., Mandrus, D. G., Hatami, F., Yao, W., Vučković, J., Majumdar, A. & Xu, X. Monolayer semiconductor nanocavity lasers with ultralow thresholds. *Nature* **520**, 69–72 (2015).
 8. Liu, C.-H., Chang, Y.-C., Norris, T. B. & Zhong, Z. Graphene photodetectors with ultra-broadband and high responsivity at room temperature. *Nat. Nanotechnol.* **9**, 273–278 (2014).
 9. Freitag, M., Low, T., Zhu, W., Yan, H., Xia, F. & Avouris, P. Photocurrent in graphene harnessed by tunable intrinsic plasmons. *Nat. Commun.* **4**, (2013).
 10. Liu, M., Yin, X., Ulin-Avila, E., Geng, B., Zentgraf, T., Ju, L., Wang, F. & Zhang, X. A graphene-based broadband optical modulator. *Nature* **474**, 64–67 (2011).
 11. Sun, Z., Martinez, A. & Wang, F. Optical modulators with 2D layered materials. *Nat. Photonics* **10**, 227–238 (2016).
 12. Havener, R. W., Zhuang, H., Brown, L., Hennig, R. G. & Park, J. Angle-Resolved Raman Imaging of Interlayer Rotations and Interactions in Twisted Bilayer Graphene. *Nano Lett.* **12**, 3162–3167 (2012).

13. Kim, K., Coh, S., Tan, L. Z., Regan, W., Yuk, J. M., Chatterjee, E., Crommie, M. F., Cohen, M. L., Louie, S. G. & Zettl, A. Raman Spectroscopy Study of Rotated Double-Layer Graphene: Misorientation-Angle Dependence of Electronic Structure. *Phys. Rev. Lett.* **108**, (2012).
14. Moon, P. & Koshino, M. Optical absorption in twisted bilayer graphene. *Phys. Rev. B* **87**, (2013).
15. Moon, P., Son, Y.-W. & Koshino, M. Optical absorption of twisted bilayer graphene with interlayer potential asymmetry. *Phys. Rev. B* **90**, (2014).
16. Havener, R. W., Liang, Y., Brown, L., Yang, L. & Park, J. Van Hove Singularities and Excitonic Effects in the Optical Conductivity of Twisted Bilayer Graphene. *Nano Lett.* **14**, 3353–3357 (2014).
17. Liang, Y., Soklaski, R., Huang, S., Graham, M. W., Havener, R., Park, J. & Yang, L. Strongly bound excitons in gapless two-dimensional structures. *Phys. Rev. B* **90**, (2014).
18. Patel, H., Havener, R. W., Brown, L., Liang, Y., Yang, L., Park, J. & Graham, M. W. Tunable Optical Excitations in Twisted Bilayer Graphene Form Strongly Bound Excitons. *Nano Lett.* **15**, 5932–5937 (2015).
19. Kim, C.-J., Sánchez-Castillo, A., Ziegler, Z., Ogawa, Y., Noguez, C. & Park, J. Chiral atomically thin films. *Nat. Nanotechnol.* **11**, 520–524 (2016).
20. Yeh, C.-H., Lin, Y.-C., Chen, Y.-C., Lu, C.-C., Liu, Z., Suenaga, K. & Chiu, P.-W. Gating Electron–Hole Asymmetry in Twisted Bilayer Graphene. *ACS Nano* **8**, 6962–6969 (2014).
21. Chung, T.-F., He, R., Wu, T.-L. & Chen, Y. P. Optical Phonons in Twisted

- Bilayer Graphene with Gate-Induced Asymmetric Doping. *Nano Lett.* **15**, 1203–1210 (2015).
22. Rivera, P., Schaibley, J. R., Jones, A. M., Ross, J. S., Wu, S., Aivazian, G., Klement, P., Seyler, K., Clark, G., Ghimire, N. J., Yan, J., Mandrus, D. G., Yao, W. & Xu, X. Observation of long-lived interlayer excitons in monolayer MoSe₂–WSe₂ heterostructures. *Nat. Commun.* **6**, 6242 (2015).
23. Klein, J., Wierzbowski, J., Regler, A., Becker, J., Heimbach, F., Müller, K., Kaniber, M. & Finley, J. J. Stark Effect Spectroscopy of Mono- and Few-Layer MoS₂. *Nano Lett.* **16**, 1554–1559 (2016).
24. Brown, L., Lochocki, E. B., Avila, J., Kim, C.-J., Ogawa, Y., Havener, R. W., Kim, D.-K., Monkman, E. J., Shai, D. E., Wei, H. I., Levendorf, M. P., Asensio, M., Shen, K. M. & Park, J. Polycrystalline Graphene with Single Crystalline Electronic Structure. *Nano Lett.* **14**, 5706–5711 (2014).
25. Sanchez-Yamagishi, J. D., Taychatanapat, T., Watanabe, K., Taniguchi, T., Yacoby, A. & Jarillo-Herrero, P. Quantum Hall Effect, Screening, and Layer-Polarized Insulating States in Twisted Bilayer Graphene. *Phys. Rev. Lett.* **108**, (2012).
26. Miller, D. A. B., Chemla, D. S., Damen, T. C., Gossard, A. C., Wiegmann, W., Wood, T. H. & Burrus, C. A. Band-Edge Electroabsorption in Quantum Well Structures: The Quantum-Confined Stark Effect. *Phys. Rev. Lett.* **53**, 2173–2176 (1984).
27. Miller, D. A. B., Chemla, D. S., Damen, T. C., Gossard, A. C., Wiegmann, W., Wood, T. H. & Burrus, C. A. Electric Field Dependence of Optical Absorption

- Near The Band Gap of Quantum-Well Structures. *Phys. Rev. B* **32**, 1043–1060 (1985).
28. Bar-Joseph, I., Klingshirn, C., Miller, D. A. B., Chemla, D. S., Koren, U. & Miller, B. I. Quantum-confined Stark effect in InGaAs/InP quantum wells grown by organometallic vapor phase epitaxy. *Appl. Phys. Lett.* **50**, 1010–1012 (1987).
29. Mak, K. F., da Jornada, F. H., He, K., Deslippe, J., Petrone, N., Hone, J., Shan, J., Louie, S. G. & Heinz, T. F. Tuning Many-Body Interactions in Graphene: The Effects of Doping on Excitons and Carrier Lifetimes. *Phys. Rev. Lett.* **112**, (2014).
30. Gao, S., Liang, Y., Spataru, C. D. & Yang, L. Dynamical Excitonic Effects in Doped Two-Dimensional Semiconductors. *Nano Lett.* **16**, 5568–5573 (2016).

CHAPTER FOUR

Two-Dimensional Material Tunnel Barrier for Josephson Junctions and Superconducting Qubits

4.1. Introduction

Recent developments in the device architecture and operation of state-of-the-art superconducting qubits has allowed the technology to initiate practical applications in quantum computing.¹⁻⁵ At the center of such qubit is the Josephson junction, which is composed of two superconductors (SCs) separated by an ultrathin tunnel barrier (Figure 4.1). Currently, the tunnel barrier for Josephson junctions is mostly fabricated using AlO_x that is natively grown on Al, as the existing fabrication method for such structure provides high quality junctions for superconducting qubits to achieve excellent coherence time.⁴ However, AlO_x has been reported to have thickness inhomogeneity⁶ and defects that may compromise the qubit performance⁷⁻⁹. Moreover, new materials with different properties for fabricating Josephson junctions are expected to introduce novel functionalities and circuit elements for superconducting

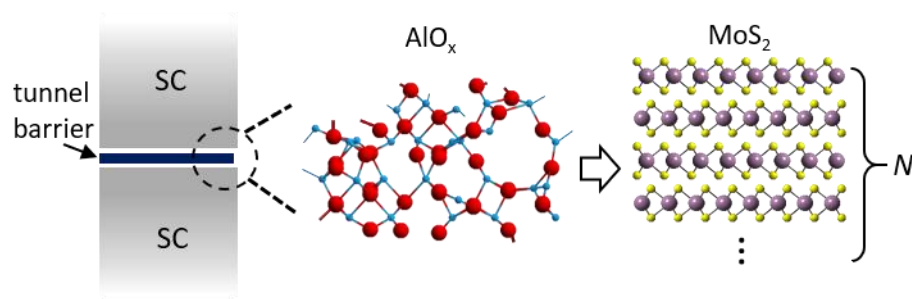


Figure 4.1 Schematics of the structure of a Josephson junction, wherein an ultrathin tunnel barrier is sandwiched between two superconductors (SCs). The barrier is mostly made of amorphous aluminum oxide natively grown on aluminum. In this work, we replace the barrier material with N -layer MoS_2 , where the number of layers N can be designed via layer-by-layer stacking.

¹This work is published on *Nano Lett.* (2019), <https://doi.org/10.1021/acs.nanolett.9b03886>.

qubits. As such, intensive efforts to implement new materials in Josephson junctions have emerged recently. This includes directly replacing the tunnel barrier such as the Re/epitaxial sapphire/Al and NbN/AlN/NbN vertical junctions^{10,11}, as well as utilizing a lateral Josephson junction geometry to implement nanowires/nanotubes¹²⁻¹⁴, two-dimensional (2D) electron gas¹⁵, and graphene¹⁶ as the weak link for new functionalities such as voltage-tunable qubits.

Two-dimensional materials could provide excellent solid-state systems for generating novel tunnel barriers for Josephson junctions with their wide varieties of electrical and magnetic properties.¹⁷⁻¹⁹ The atomic thinness of monolayer 2D materials (~a few Å) allows them to be used as tunnel barriers. Their van der Waals layered structures further enable the precise design of the barrier thickness through layer-by-layer stacking, whereby each layer can be a different 2D material to generate a heterostructure barrier. In addition, they can be released from the substrate as a freestanding atomically thin film, making it possible to combine 2D materials with different SCs. These unique properties would allow for the design of the tunnel barrier band structure using 2D materials with different band gaps and band offsets²⁰, the study of Josephson junction in the ultimately short regime²¹, and the fabrication of novel quantum circuit components such as π -junctions using 2D magnets²²⁻²⁴. Nevertheless, as most of the common SCs are easily oxidized, it is essential to have a method that can maintain oxide-free interfaces between the SCs and the 2D material barrier while keeping the advantages of the above designability and being scalable to a technologically relevant scale. In this Chapter, we demonstrate the Josephson junctions with a 2D material barrier using Al/MoS₂/Al tunnel junctions as an example

(Figure 4.1, right). We first present our process, named as barrier-first method, that provides a scalable fabrication solution for integrating 2D materials with oxygen-sensitive bulk SCs. The Josephson effect in these MoS₂-based tunnel junctions are then demonstrated, where the critical current can be tuned over orders of magnitudes through layer-by-layer stacking of MoS₂ monolayers. Finally, we demonstrate the engineering and operation of superconducting qubits with a MoS₂ tunnel barrier for the first time.

4.2. The Barrier-First Method

The concept of our barrier-first method is described in Figure 4.2a. We start with large-scale monolayers of MoS₂ that are grown by metal-organic chemical vapor deposition (MOCVD) on SiO₂/Si substrates, and stack them layer-by-layer in a vacuum chamber (<50 mTorr) until we reach the targeted number of layers N for the designed thickness of the tunnel barrier (step **i**). The details of the large-scale growth and vacuum stacking have been reported in Chapter 2 and our previous work^{20,25} and. In step **ii**, we define the first superconducting electrodes (SC1) by directly evaporating Al metal onto the stacked MoS₂ using a shadow mask. In step **iii**, the Al-on-MoS₂ thin film is released from the substrate, flipped over, and transferred onto the final substrate (sapphire). The SC1 now becomes the bottom electrode, where the MoS₂ side is exposed on top. The MoS₂ film here provides the needed encapsulation of the bottom aluminum from the air and various chemicals in the following process besides serving as the tunnel barrier. In step **iv**, we directly evaporate aluminum onto the MoS₂ again and define the second electrodes (SC2) using standard photolithography

and reactive-ion etching. An airbridge (see Figure A4.1 in the appendix) is fabricated to gain access to the junction without using a dielectric as a spacer to separate the top electrodes from the bottom electrodes in order to reduce the microwave loss during qubit measurement.

As illustrated, we start with making the tunnel barrier instead of growing it on top of the bottom electrodes as commonly done. This reversed process sequence provides us with three key advantages. First, it allows us to design the barrier structure independently of the electrodes. Second, by directly depositing SC electrodes on either side, oxide contamination at the barrier/ electrode interfaces are avoided, as shown in

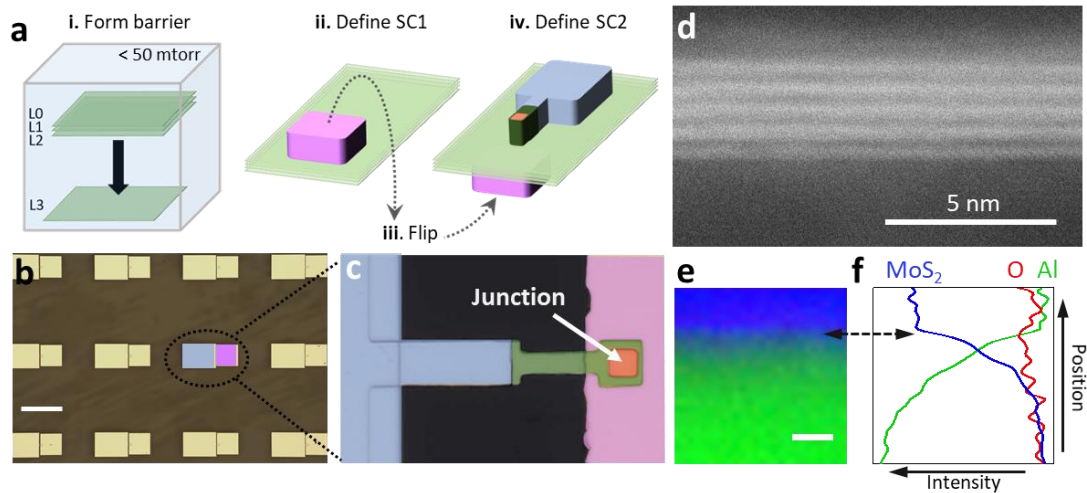


Figure 4.2 The barrier-first method. **a**, Fabrication steps for the barrier-first method. See main text for a detailed description. **b**, An optical image of a batch-fabricated Al/4L-MoS₂/Al Josephson junction array. The circled device is false-colored, where the purple is the bottom electrode or SC1, and the blue is the top electrode or SC2. The scale bar is 0.4 mm. **c**, Zoom-in image of an Al/4L-MoS₂/Al Josephson junction. Blue: top electrode pad; green: suspended aluminum airbridge; red: the Al/MoS₂/Al junction; purple: bottom electrode. Junction size is 5 by 5 μm². **d**, Cross-sectional HAADF STEM image of an Al/5L-MoS₂/Al junction. The five bright lines in the middle are the vacuum-stacked MoS₂. **e**, Elemental mapping across the bottom interface of the junction. Green: Al (from EELS), red: O (from EELS), blue: MoS₂ (from ADF intensity). The scale bar is 2 nm. The arrow marks the Al/MoS₂ interface. **f**, Signal intensity versus location corresponding to **e**. Colors for each element are the same as in **e**.

Figure 4.2d-f below. Third, as the MoS₂ tunnel barrier is generated by stacking wafer-scale MoS₂ monolayers layer-by-layer, the barrier thickness is precisely controlled on the large scale and the devices can be batch fabricated as arrays. An optical microscope image of the as-fabricated junction array is presented in Figure 4.2b. The detailed structure of the Al/MoS₂/Al tunnel device is shown in the false-colored zoom-in image in Figure 4.2c, which includes the top (blue) and bottom (purple) electrode, an airbridge (green) and the tunnel junction (red, 5 by 5 μm²).

Figure 4.2d-f confirm that the barrier-first method maintains oxide free interfaces between the MoS₂ and Al, as the MoS₂ barrier film protects the bottom Al throughout the fabrication process until the evaporation of top Al, (i.e. in steps **iii** and **iv**.) Figure 4.2d first shows a cross-sectional high-angle annular dark-field (HAADF) STEM image of an Al/5L-MoS₂/Al junction. (See appendix for remarks on sample preparation.) The 5L-MoS₂ appears in the image as the five bright lines in the middle, where the monolayer thickness is roughly 0.64 nm. As shown, all MoS₂ layers are parallel to each other without defects and show clean interlayer interfaces, demonstrating the quality of our vacuum-stacked MoS₂ barrier. The chemical compositions across the bottom interface between MoS₂ and aluminum are further characterized using electron energy loss spectroscopy (EELS). Figure 4.2e shows the elemental map with colors representing Al (green, from EELS), O (red, from EELS) and MoS₂ (blue, from ADF intensity), and Figure 4.2f presents the corresponding signal intensity from each element along the vertical axis. It is observed that the Al (Mo) signal intensity roughly reaches minimum (maximum) around the Al/MoS₂ interface, and the O signal remains close to the noise level everywhere across the

interface. This evidence supports that there is no oxide contamination at the interface between MoS₂ and Al, confirming that we have successfully maintained intrinsic interfaces in our Al/MoS₂/Al junctions.

We note that we have only shown that the bottom MoS₂/Al interface is oxide-free from our cross-sectional images in Figure 4.2, because we observe significant damages to the top electrode of the junction during cross-section sample preparation. (MoS₂ and bottom electrodes remain intact with careful optimization.) This damage likely comes from the beam drift during cutting/thinning the sample using focused ion beam with Ga ion due to the insulating sapphire substrate used. However, we emphasize that the interface of concern in our junction fabrication is the bottom interface, because only the MoS₂/bottom Al has gone through multiple processes after the first Al deposition and thus is exposed to an oxidizing environment. In contrast, the top electrode is evaporated under 2×10^{-8} Torr in the last step with a thickness of 320 nm, which completely encapsulates the interface inside the vacuum.

4.3. Tunable Josephson Current via Layer-by-Layer Assembly

We now discuss the electrical properties and DC Josephson effect of the as-fabricated Al/MoS₂/Al junctions. At room temperature, all Al/NL-MoS₂/Al junctions ($N=3, 4, 5$) exhibit the characteristic nonlinear J-V curves of normal tunneling as shown in Figure 3a. The current decreases exponentially (\sim a factor of five) with each additional layer in the barrier, which again agrees with the exponential dependence of tunnel current on the thickness of the barrier. We further characterize the low temperature properties of the junctions in a dilution fridge at 25 mK and observe a

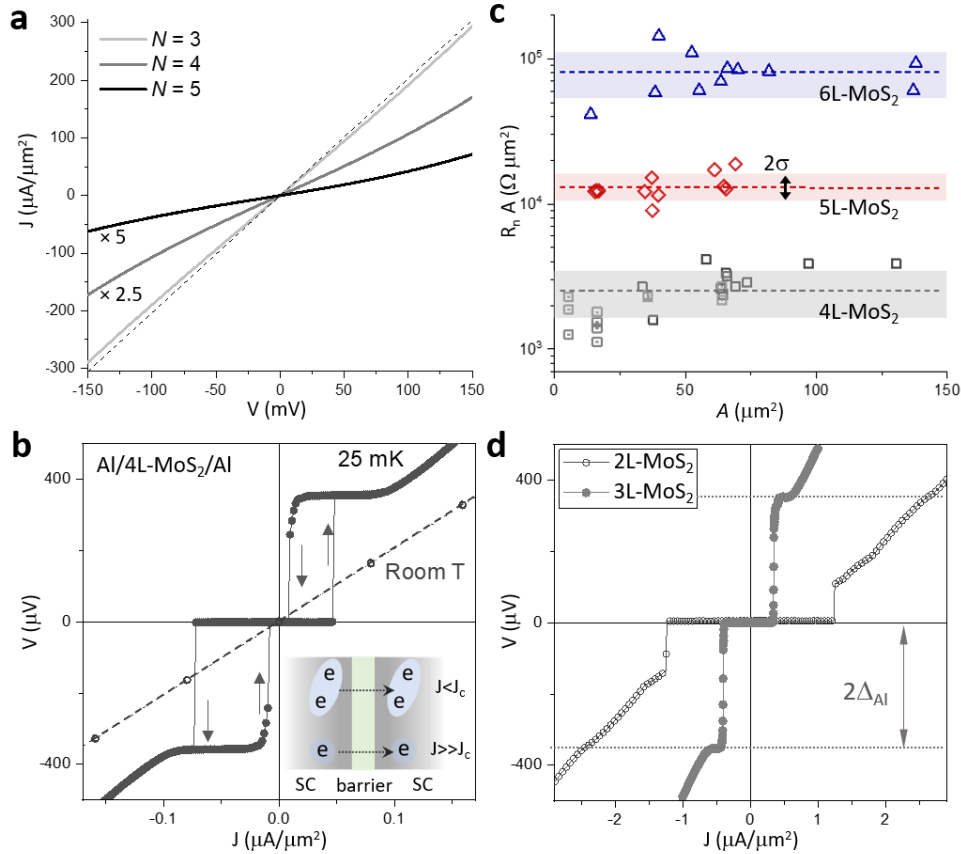


Figure 4.3 Electrical characterization and Josephson effect. **a**, Room temperature J-V curves of junctions with different N , where $N=3, 4, 5$. The values of the current density is multiplied by 1, 2.5 and 5, respectively, for clarity. The dashed line is a straight line for reference. **b**, J-V curves of an Al/4L-MoS₂/Al tunnel junction at room temperature (empty dots) and 25 mK (solid). The arrows indicate the current sweeping directions, starting from zero to positive bias. Inset: Schematics of the Josephson effect and normal tunneling at different current biases. **c**, Resistance-area product ($R_n A$) versus junction area (A) of MoS₂ junctions with $N=4, 5, 6$. σ is the standard deviation and the color bands denote 2σ of each N . Note that the 4L-MoS₂ data set includes two batches of devices, which are shown with different symbols, squares and squares with dots. σ for the 4L-MoS₂ devices includes both batches. **d**, Josephson curves of Al/NL-MoS₂/Al with $N=2$ and 3 , where both curves are measured from positive to negative current bias. Δ_{Al} is the superconducting gap of Al.

dramatic transition of the J-V curve in the zero-bias regime as displayed in Figure 4.3b, which is measured from a representative 4L-MoS₂ device. Four distinct features are clearly shown in stark contrast to that at room temperature in this low bias regime:

(1) there is a finite current up to a critical current density J_c at $V=0$, (2) an abrupt switch from zero voltage to roughly $\pm 350 \mu\text{V}$ after J_c , (3) behavior similar to that at room temperature as the current bias is further increased, and (4) the J-V curves show hysteresis depending on the current sweeping directions.

The first three features are characteristic of the Josephson effect across a tunnel barrier as illustrated in the inset schematics of Figure 4.3b. Below J_c , the Cooper pair can directly tunnel through the barrier without energy dissipation, and thus no finite voltage is measured (i.e. the DC Josephson effect). Once the current bias exceeds J_c , excess current can only be carried by generating quasiparticles for tunneling. This requires a voltage that is twice the size of the superconducting gap (2Δ), which is the voltage the device reaches after J_c . We can accordingly estimate 2Δ of our aluminum to be $350 \mu\text{V}$, consistent with the reported value for bulk Al²⁶. At a voltage much larger than 2Δ , normal single particle tunneling that happens at room temperature dominates current transport again. The hysteresis, on the other hand, results from the underdamped nature of our junction circuits²⁷. The results presented above directly demonstrate that we have successfully fabricated Josephson junctions with the Al/MoS₂/Al vertical structure.

Precise control of the tunnel resistance and Josephson current is essential to engineer superconducting qubits with proper quantum states for operation. This can be realized with a large tuning range and high fidelity through controlling the layer number N of MoS₂. Figure 4.3c presents the zero-bias tunnel resistance-area product ($R_n A$) of different N and junction area A . For devices with the same N , $R_n A$ remains approximately constant as expected for tunnel junctions (dashed lines). For devices

with the same A , $R_n A$ can be tuned by orders of magnitudes by varying N . As shown by the Al/5L-MoS₂/Al junction array, which is batch-fabricated over a 5 by 5 mm² area on a single chip, we can achieve good homogeneity with a standard deviation σ that is 17% of the average tunnel resistance of the array. This spread is significantly smaller compared to the factor of five change when adding or reducing one layer of MoS₂ in the barrier. As the critical current I_c of a Josephson junction is proportional to Δ/R_n , the I_c also depends on N exponentially. This is demonstrated in Figure 4.3d, where we show that the J_c of 2L-MoS₂ tunnel barrier is $\sim 1.2 \mu\text{A}/\mu\text{m}^2$, 3L-MoS₂ $\sim 0.36 \mu\text{A}/\mu\text{m}^2$ and 4L-MoS₂ $\sim 0.04 \mu\text{A}/\mu\text{m}^2$ (from Figure 4.3b). Accordingly, one can design the I_c of a junction with N and A as the two independent variables, i.e. $I_c(N, A) = J_c(N) \times A$, which scales exponentially with N but linearly with A . This layer-by-layer tunability for designing the I_c makes the MoS₂ barrier a useful material system for engineering superconducting qubits as shown in Figure 4.4.

We briefly note here that we observe a crossover of our Al/ N L-MoS₂/Al junctions from a superconductor-insulator-superconductor (SIS) junction for $N \geq 3$ to a superconductor-normal metal-superconductor (SNS) junction for $N = 2$. This can be seen by the switching after I_c , as the voltage immediately reaches $V = \pm 2\Delta_{\text{Al}}$ for $N \geq 3$, while it reaches sub-gap values for $N = 2$. Figure A4.2 further shows multiple Andreev reflection peaks for $N = 2$, which are absent for $N \geq 3$. Such crossover depending on N may be due to the semiconducting nature of our tunnel barrier. MoS₂ has a much smaller bandgap (~ 1.9 eV for monolayer and lower for multilayers) than other common barriers such as AlO_x (4-9 eV²⁸), which makes the band profile of the

junction more sensitive to the geometry²⁹⁻³¹. The details of the cross-over, however, are beyond the scope of this thesis and thus will be studied in the future.

4.4. *MoS₂ Superconducting Qubits*

With I_c being a function of (N, A) , we can now design the parameters for the Al/MoS₂/Al superconducting qubits accordingly. For instance, in a transmon qubit, the transition energy from the ground state $|g\rangle$ to the first excited state $|e\rangle$ is $E = \sqrt{8E_J E_c} - E_c$, where $E_J = \hbar I_c / 2e_0$ is the Josephson energy, e_0 is the electron charge, and $E_c = e_0^2 / 2C$ is the capacitive energy of the overall circuit shown in the circuit diagram of Figure 4.4a (inset). Designing E , therefore, can be achieved by choosing (N, A) for E_J , and adjusting E_c using the overall circuit capacitance in addition to the Josephson junction capacitance. In Figure 4.4, we fabricate a single Al/4L-MoS₂/Al Josephson junction with a junction area of 2 by 2 μm^2 on a sapphire substrate, which gives us a transition frequency $f_q = E/h = 3.94$ GHz between the lowest energy states. As indicated by the yellow arrow in Figure 4.4a, the junction is placed at the center of an aluminum microwave bulk cavity resonator designed to have a resonance frequency at $f_r = 7.107$ GHz as determined by the dimensions of the cavity. The coupling strength g between the MoS₂ qubit and the resonator is determined by the geometry of the electrodes of the MoS₂ qubit, which is designed to be ~ 60 MHz in our experiment based on black box quantization³². As $g \ll f_r - f_q$, the qubit and the resonator are coupled in the dispersive regime.

To confirm the coupling between the qubit and the resonator, we first measure the response of the system by sweeping the microwave frequency around f_r while

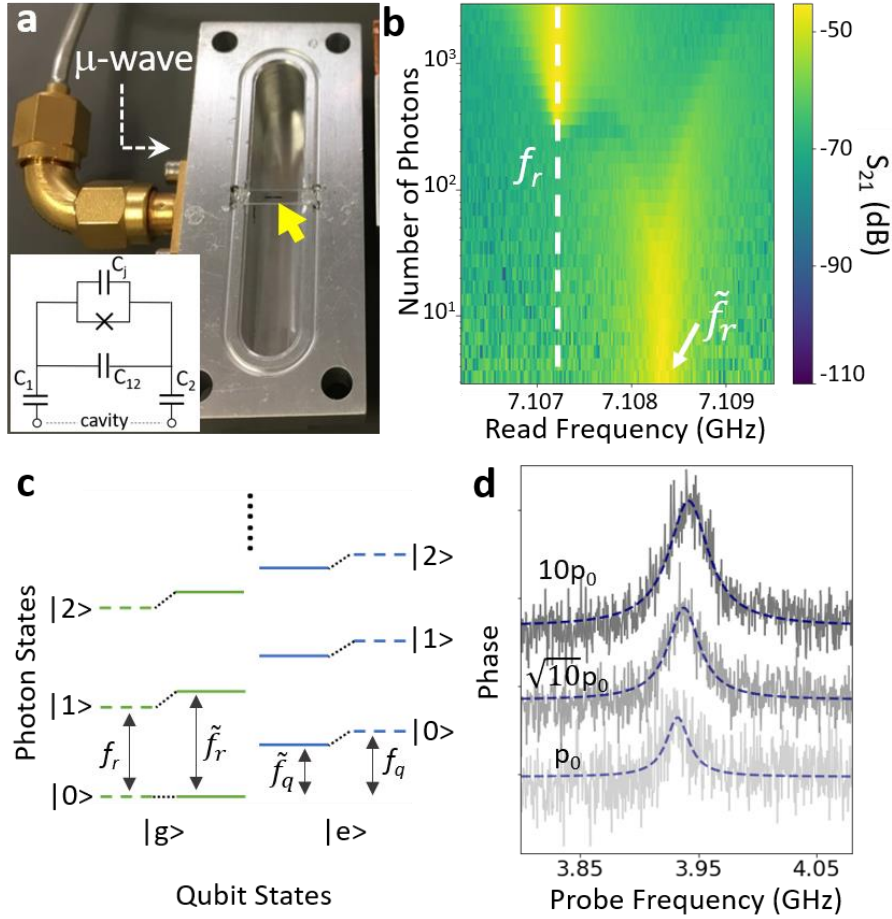


Figure 4.4 A superconducting qubit with a MoS₂ tunnel barrier. **a**, The measurement setup. Microwave tones are input using a coaxial cable to the aluminum resonator as indicated, while the signal is collected from a second cable on the lid (not shown). The yellow arrow indicates the Al/4L-MoS₂/Al Josephson junction and the capacitor pads. Inset: An effective circuit diagram for the setup. C_1 , C_2 are the capacitance of the pads and C_{12} is the inter-pad capacitance. **b**, The response of the qubit-resonator system as a function of the applied microwave power. The lower frequency peak corresponds to the cavity frequency f_r without hybridization with the qubit, while the higher frequency peak \tilde{f}_r corresponds to the resonance with hybridization. **c**, Schematic of the quantum states that contribute to the response in **b**. $|i\rangle$ with $i=0, 1, 2$ are the photon number states of the resonator, while $|g\rangle$, $|e\rangle$ denote the ground and first excited states of the qubit. The dashed (solid) lines denote the bare (dressed) states of the system before (after) hybridization. **d**, Qubit excitation at different excitation powers, where p_0 is the probe power at the sample and is $\sim 8 \times 10^{-10}$ mW. Dashed lines are fits to Lorentzian peaks.

increasing the photon number in the cavity by varying the applied microwave power

as shown in Figure 4.4b. For small photon number ($\ll 100$), we see a single peak at around 7.108 GHz (denoted as \tilde{f}_r). In the intermediate regime, the response splits into two peaks, of which the splitting increases and intensity decreases as the photon number further increased. Eventually, at large photon number, the peak jumps to f_r . The above power dependence is characteristic of the hybridization arising from the Jaynes-Cummings interaction between a resonator and a qubit³³. Figure 4.4c illustrates the quantum states of the qubit-resonator system, and the dashed (solid) lines denote the bare (dressed) states of the system before (after) their hybridization. Near the single photon power at the device, \tilde{f}_r corresponds to the excitation from the ground to the lowest excited state of the qubit-resonator hybrid system, i.e. ($|g\rangle |1\rangle + \frac{g}{f_r - f_q} |e\rangle |0\rangle$). As the photon number increases, the system enters a region of semiclassical bistability that presumably contributes to the observed power dependence as previously reported³³. Above the critical photon number, the system frequency is no longer dressed by the qubit-resonator interaction and becomes insensitive to the qubit state. The experiment above indicates the successful coupling of the MoS₂ qubit to the bulk microwave resonator, with behavior that is well understood with existing theory. This allows us to operate and readout the MoS₂ transmon with established techniques in superconducting circuit quantum electrodynamics (QED).

In Figure 4.4d, we further demonstrate the manipulation of the MoS₂ qubit by using a microwave drive tone at the qubit dressed state frequency \tilde{f}_q , to alter the qubit states, while reading the state of the qubit with a readout microwave tone at \tilde{f}_r in the low photon number region. We measure the phase shift of the readout tone as the drive

tone is swept around \tilde{f}_q . Indeed, the qubit transition is observed as a large phase shift when the microwave sweeps through \tilde{f}_q , showing that we have put the qubit into the excited state. As the excitation power is increased, the peak is significantly broadened as a result of the stimulated relaxation of the qubit due to the applied \tilde{f}_q microwave tone ($p_0 \sim 8 \times 10^{-10}$ mW). We measure the power dependence of the peak and extrapolate for the peak width at zero-power. This gives us an estimate of the coherence time T_2^* , which is ~ 12 ns for the device measured.

Here, we propose three sources that may have contributed to the relatively short coherence time of our MoS₂ qubits as well as potential solutions to address them to improve the coherent time. The first source is the device geometry. As an example, our large junction size (2 by 2 μm^2) based on the photolithography process is two orders of magnitudes larger than those of typical AlO_x transmon qubits ($(\sim \text{hundreds})^2$ nm). In previous reports on AlO_x phase qubits, the energy relaxation time (T_1) in larger AlO_x junctions ($>70 \mu\text{m}^2$) was 10 - 20 ns, mainly limited by the number of two-level systems in the barrier. It is shown to improve by reducing the junction size until other decoherence sources dominate^{34,35}. For our qubits, shrinking the junction area may have the same positive effect, while the reduced E_J due to the smaller junction area can be compensated by adjusting the N of the barrier or switching to another 2D material that forms a lower tunnel barrier height. The second possible source is the unoptimized fabrication process. For example, the use of photoresist to define the contact between top aluminum and the MoS₂ tunnel barrier would leave polymer residues that degrade the junction quality³⁶. Such residue may be reduced by, for

instance, Ar/H₂ annealing of the top interface before evaporation³⁷. Lastly, the dielectric loss of the MOCVD-grown MoS₂ may contribute to decoherence, such as due to the presence of defects. Currently, the defect characteristics and the microwave properties of 2D materials are not well-understood in the low temperature (25 mK) and low power (near single photon) regimes where qubits operate, in part hindered by the underdeveloped fabrication method for suitable devices³⁸. Our work, hence, may provide a viable way to study such properties of 2D materials in this previously inaccessible regime.

4.5. Summary

In conclusion, we have fabricated Josephson junctions and superconducting qubits made with MoS₂ tunnel barriers using our barrier-first method. The junction and qubit properties can be precisely tuned layer-by-layer by exploiting the van der Waals layered structure of MoS₂ to design the barrier thickness. Our method opens up the possibility of making designable Josephson junctions with a MoS₂ tunnel barrier, and can potentially be applied to other similar 2D materials such as WSe₂ and hBN, each having a distinct band gap, band offset, and other physical properties. In the future, this may be generalized to other combinations of superconductors and 2D materials including 2D magnets for fabricating π -Josephson junctions. Our method here will provide a powerful platform to study the effects of different material properties in superconducting qubit circuits under different geometries, and to explore new device structures that could lead to novel quantum circuit components for quantum computing.

4.6. Appendix

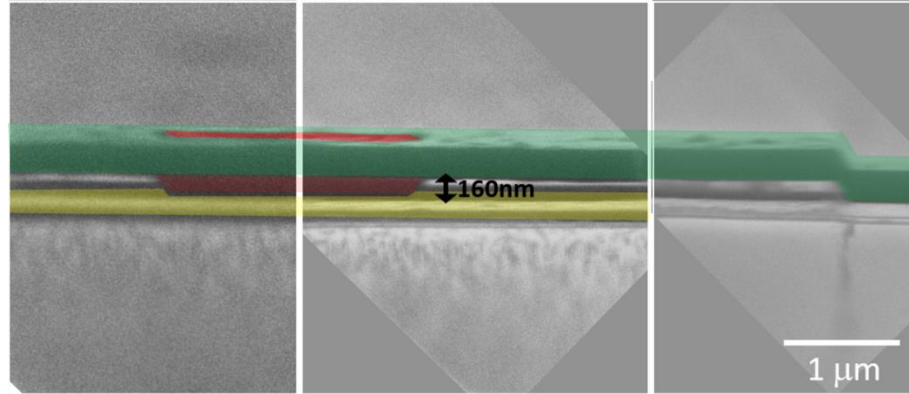


Figure A4.1 SEM image of the suspended airbridge. Image is false-colored: green, the Al airbridge connected to the rest of the top electrode. Red: the Al/MoS₂/Al junction. Yellow: bottom electrode. The airbridge is suspended 160 nm above the bottom electrode.

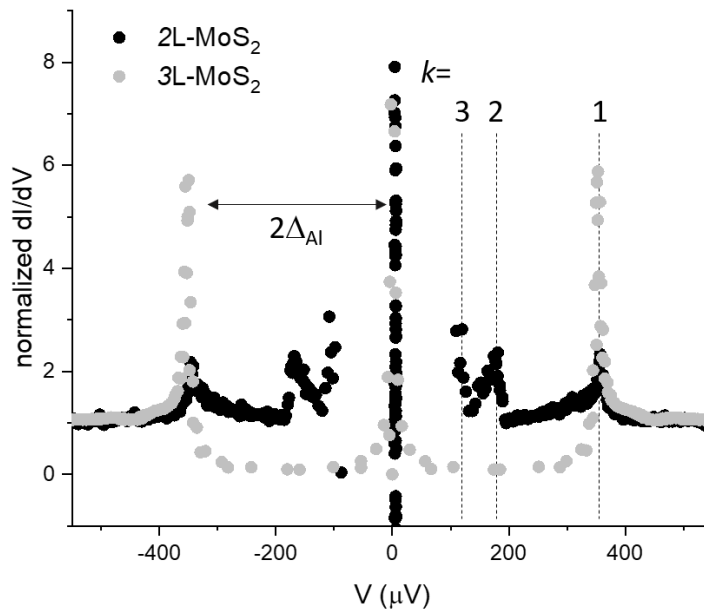


Figure A4.2. Normalized dI/dV curves of 2L and 3L-MoS₂ barrier as a function of V . Each dI/dV curve is normalized to the normal state conductance. k denotes the number of the Andreev reflections; Andreev reflection peaks appear at $V=2\Delta_{Al}/k$, $k=1, 2, 3$.

4.7. References

- (1) Wallraff, A.; Schuster, D. I.; Blais, A.; Frunzio, L.; Huang, R. -S.; Majer, J.;

- Kumar, S.; Girvin, S. M.; Schoelkopf, R. J. Strong Coupling of a Single Photon to a Superconducting Qubit Using Circuit Quantum Electrodynamics. *Nature* **2004**, *431* (7005), 162–167. <https://doi.org/10.1038/nature02851>.
- (2) Koch, J.; Yu, T. M.; Gambetta, J.; Houck, A. A.; Schuster, D. I.; Majer, J.; Blais, A.; Devoret, M. H.; Girvin, S. M.; Schoelkopf, R. J. Charge-Insensitive Qubit Design Derived from the Cooper Pair Box. *Phys. Rev. A* **2007**, *76* (4), 042319. <https://doi.org/10.1103/PhysRevA.76.042319>.
- (3) Buluta, I.; Nori, F. Quantum Simulators. *Science* **2009**, *326* (5949), 108–111. <https://doi.org/10.1126/science.1177838>.
- (4) Devoret, M. H.; Schoelkopf, R. J. Superconducting Circuits for Quantum Information: An Outlook. *Science* **2013**, *339* (6124), 1169–1174. <https://doi.org/10.1126/science.1231930>.
- (5) Neill, C.; Roushan, P.; Kechedzhi, K.; Boixo, S.; Isakov, S. V.; Smelyanskiy, V.; Megrant, A.; Chiaro, B.; Dunsworth, A.; Arya, K.; Barends, R.; Burkett, B.; Chen, Y.; Chen, Z.; Fowler, A.; Foxen, B.; Giustina, M.; Graff, R.; Jeffrey, E.; Huang, T.; Kelly, L.; Klimov, P.; Lucero, E.; Mutus, J.; Neeley, M.; Quintana, C.; Sank, D.; Vainsencher, A.; Wenner, J.; White, T. C.; Neven, H.; Martinis, J. M. A Blueprint for Demonstrating Quantum Supremacy with Superconducting Qubits. *Science* **2018**, *360* (6385), 195–199. <https://doi.org/10.1126/science.aao4309>.
- (6) Zeng, L. J.; Nik, S.; Greibe, T.; Krantz, P.; Wilson, C. M.; Delsing, P.; Olsson, E. Direct Observation of the Thickness Distribution of Ultrathin AlO_x Barriers in Al/AlO_x/Al Josephson Junctions. *J Phys Appl Phys* **2015**, *48* (39), 395308. <https://doi.org/10.1088/0022-3727/48/39/395308>.

- (7) Oliver, W. D.; Welander, P. B. Materials in Superconducting Quantum Bits. *MRS Bull.* **2013**, *38* (10), 816–825. <https://doi.org/10.1557/mrs.2013.229>.
- (8) McDermott, R. Materials Origins of Decoherence in Superconducting Qubits. *IEEE Trans. Appl. Supercond.* **2009**, *19* (1), 2–13. <https://doi.org/10.1109/TASC.2008.2012255>.
- (9) Klimov, P. V.; Kelly, J.; Chen, Z.; Neeley, M.; Megrant, A.; Burkett, B.; Barends, R.; Arya, K.; Chiaro, B.; Chen, Y.; Dunsworth, A.; Fowler, A.; Foxen, B.; Gidney, C.; Giustina, M.; Graff, R.; Huang, T.; Jeffrey, E.; Lucero, E.; Mutus, J. Y.; Naaman, O.; Neill, C.; Quintana, C.; Roushan, P.; Sank, D.; Vainsencher, A.; Wenner, J.; White, T. C.; Boixo, S.; Babbush, R.; Smelyanskiy, V. N.; Neven, H.; Martinis, J. M. Fluctuations of Energy-Relaxation Times in Superconducting Qubits. *Phys. Rev. Lett.* **2018**, *121* (9), 090502. <https://doi.org/10.1103/PhysRevLett.121.090502>.
- (10) Oh, S.; Cicak, K.; Kline, J. S.; Sillanpaa, M. A.; Osborn, K. D.; Whittaker, J. D.; Simmonds, R. W.; Pappas, D. P. Elimination of Two Level Fluctuators in Superconducting Quantum Bits by an Epitaxial Tunnel Barrier. *Phys. Rev. B* **2006**, *74* (10). <https://doi.org/10.1103/PhysRevB.74.100502>.
- (11) Nakamura, Y.; Terai, H.; Inomata, K.; Yamamoto, T.; Qiu, W.; Wang, Z. Superconducting Qubits Consisting of Epitaxially Grown NbN/AlN/NbN Josephson Junctions. *Appl. Phys. Lett.* **2011**, *99* (21), 212502. <https://doi.org/10.1063/1.3663539>.
- (12) Larsen, T. W.; Petersson, K. D.; Kuemmeth, F.; Jespersen, T. S.; Krogstrup, P.; Nygård, J.; Marcus, C. M. Semiconductor-Nanowire-Based Superconducting

- Qubit. *Phys. Rev. Lett.* **2015**, *115* (12), 127001.
<https://doi.org/10.1103/PhysRevLett.115.127001>.
- (13) de Lange, G.; van Heck, B.; Bruno, A.; van Woerkom, D. J.; Geresdi, A.; Plissard, S. R.; Bakkers, E. P. A. M.; Akhmerov, A. R.; DiCarlo, L. Realization of Microwave Quantum Circuits Using Hybrid Superconducting-Semiconducting Nanowire Josephson Elements. *Phys. Rev. Lett.* **2015**, *115* (12), 127002.
<https://doi.org/10.1103/PhysRevLett.115.127002>.
- (14) Mergenthaler, M.; Nersisyan, A.; Patterson, A.; Esposito, M.; Baumgartner, A.; Schönenberger, C.; Briggs, G. A. D.; Laird, E. A.; Leek, P. J. Realization of a Carbon-Nanotube-Based Superconducting Qubit. *ArXiv190410132 Cond-Mat Physicsquant-Ph* **2019**.
- (15) Casparis, L.; Connolly, M. R.; Kjaergaard, M.; Pearson, N. J.; Kringhøj, A.; Larsen, T. W.; Kuemmeth, F.; Wang, T.; Thomas, C.; Gronin, S.; Gardner, G. C.; Manfra, M. J.; Marcus, C. M.; Petersson, K. D. Superconducting Gatemon Qubit Based on a Proximitized Two-Dimensional Electron Gas. *Nat Nanotechnol* **2018**, *13* (10), 915–919. <https://doi.org/10.1038/s41565-018-0207-y>.
- (16) Wang, J. I. -J.; Rodan-Legrain, D.; Bretheau, L.; Campbell, D. L.; Kannan, B.; Kim, D.; Kjaergaard, M.; Krantz, P.; Samach, G. O.; Yan, F.; Yoder, J. L.; Watanabe, K.; Taniguchi, T.; Orlando, T. P.; Gustavsson, S.; Jarillo-Herrero, P.; Oliver, W. D. Coherent Control of a Hybrid Superconducting Circuit Made with Graphene-Based van Der Waals Heterostructures. *Nat. Nanotechnol.* **2018**, *1*.
<https://doi.org/10.1038/s41565-018-0329-2>.
- (17) Novoselov, K. S.; Jiang, D.; Schedin, F.; Booth, T. J.; Khotkevich, V. V.;

- Morozov, S. V.; Geim, A. K. Two-Dimensional Atomic Crystals. *Proc. Natl. Acad. Sci. U. S. A.* **2005**, *102* (30), 10451–10453.
- (18) Geim, A. K.; Grigorieva, I. V. Van Der Waals Heterostructures. *Nature* **2013**, *499* (7459), 419–425. <https://doi.org/10.1038/nature12385>.
- (19) Novoselov, K. S.; Mishchenko, A.; Carvalho, A.; Neto, A. H. C. 2D Materials and van Der Waals Heterostructures. *Science* **2016**, *353* (6298), aac9439. <https://doi.org/10.1126/science.aac9439>.
- (20) Kang, K.; Lee, K. -H.; Han, Y.; Gao, H.; Xie, S.; Muller, D. A.; Park, J. Layer-by-Layer Assembly of Two-Dimensional Materials into Wafer-Scale Heterostructures. *Nature* **2017**, *550* (7675), 229–233. <https://doi.org/10.1038/nature23905>.
- (21) Lee, G. -H.; Kim, S.; Jhi, S.-H.; Lee, H. -J. Ultimately Short Ballistic Vertical Graphene Josephson Junctions. *Nat. Commun.* **2015**, *6*, 6181. <https://doi.org/10.1038/ncomms7181>.
- (22) Huang, B.; Clark, G.; Navarro-Moratalla, E.; Klein, D. R.; Cheng, R.; Seyler, K. L.; Zhong, D.; Schmidgall, E.; McGuire, M. A.; Cobden, D. H.; Yao, W.; Xiao, D.; Jarillo-Herrero, P.; Xu, X. Layer-Dependent Ferromagnetism in a van Der Waals Crystal down to the Monolayer Limit. *Nature* **2017**, *546* (7657), 270–273. <https://doi.org/10.1038/nature22391>.
- (23) Ryazanov, V. V.; Oboznov, V. A.; Rusanov, A. Y.; Veretennikov, A. V.; Golubov, A. A.; Aarts, J. Coupling of Two Superconductors through a Ferromagnet: Evidence for a π Junction. *Phys. Rev. Lett.* **2001**, *86* (11), 2427–2430. <https://doi.org/10.1103/PhysRevLett.86.2427>.

- (24) Vávra, O.; Gaži, S.; Golubović, D. S.; Vávra, I.; Dérer, J.; Verbeeck, J.; Van Tendeloo, G.; Moshchalkov, V. V. 0 and π Phase Josephson Coupling through an Insulating Barrier with Magnetic Impurities. *Phys. Rev. B* **2006**, *74* (2), 020502. <https://doi.org/10.1103/PhysRevB.74.020502>.
- (25) Kang, K.; Xie, S.; Huang, L.; Han, Y.; Huang, P. Y.; Mak, K. F.; Kim, C. -J.; Muller, D.; Park, J. High-Mobility Three-Atom-Thick Semiconducting Films with Wafer-Scale Homogeneity. *Nature* **2015**, *520* (7549), 656–660. <https://doi.org/10.1038/nature14417>.
- (26) Kittel, C. *Introduction to Solid State Physics*, 8th ed.; Wiley, 2005.
- (27) Martinis, J. M.; Kautz, R. L. Classical Phase Diffusion in Small Hysteretic Josephson Junctions. *Phys. Rev. Lett.* **1989**, *63* (14), 1507–1510. <https://doi.org/10.1103/PhysRevLett.63.1507>.
- (28) Canulescu, S.; Rechendorff, K.; Borca, C. N.; Jones, N. C.; Bordo, K.; Schou, J.; Pleth Nielsen, L.; Hoffmann, S. V.; Ambat, R. Band Gap Structure Modification of Amorphous Anodic Al Oxide Film by Ti-Alloying. *Appl. Phys. Lett.* **2014**, *104* (12), 121910. <https://doi.org/10.1063/1.4866901>.
- (29) Kleinsasser, A. W.; Jackson, T. N.; McInturff, D.; Rammo, F.; Pettit, G. D.; Woodall, J. M. Crossover from Tunneling to Metallic Behavior in Superconductor-semiconductor Contacts. *Appl. Phys. Lett.* **1990**, *57* (17), 1811–1813. <https://doi.org/10.1063/1.104029>.
- (30) Island, J. O.; Steele, G. A.; Zant, H. S. J. van der; Castellanos-Gomez, A. Thickness Dependent Interlayer Transport in Vertical MoS₂ Josephson Junctions. *2D Mater.* **2016**, *3* (3), 031002. <https://doi.org/10.1088/2053-1583/3/3/031002>.

- (31) Liu, Y.; Guo, J.; Zhu, E.; Liao, L.; Lee, S. -J.; Ding, M.; Shakir, I.; Gambin, V.; Huang, Y.; Duan, X. Approaching the Schottky–Mott Limit in van Der Waals Metal–Semiconductor Junctions. *Nature* **2018**, *557* (7707), 696.
<https://doi.org/10.1038/s41586-018-0129-8>.
- (32) Nigg, S. E.; Paik, H.; Vlastakis, B.; Kirchmair, G.; Shankar, S.; Frunzio, L.; Devoret, M. H.; Schoelkopf, R. J.; Girvin, S. M. Black-Box Superconducting Circuit Quantization. *Phys. Rev. Lett.* **2012**, *108* (24), 240502.
<https://doi.org/10.1103/PhysRevLett.108.240502>.
- (33) Bishop, L. S.; Ginossar, E.; Girvin, S. M. Response of the Strongly Driven Jaynes-Cummings Oscillator. *Phys. Rev. Lett.* **2010**, *105* (10), 100505.
<https://doi.org/10.1103/PhysRevLett.105.100505>.
- (34) Cooper, K. B.; Steffen, M.; McDermott, R.; Simmonds, R. W.; Oh, S.; Hite, D. A.; Pappas, D. P.; Martinis, J. M. Observation of Quantum Oscillations between a Josephson Phase Qubit and a Microscopic Resonator Using Fast Readout. *Phys. Rev. Lett.* **2004**, *93* (18), 180401. <https://doi.org/10.1103/PhysRevLett.93.180401>.
- (35) Martinis, J. M.; Cooper, K. B.; McDermott, R.; Steffen, M.; Ansmann, M.; Osborn, K. D.; Cicak, K.; Oh, S.; Pappas, D. P.; Simmonds, R. W.; Yu, C. C. Decoherence in Josephson Qubits from Dielectric Loss. *Phys. Rev. Lett.* **2005**, *95* (21), 210503.
- (36) Quintana, C. M.; Megrant, A.; Chen, Z.; Dunsworth, A.; Chiaro, B.; Barends, R.; Campbell, B.; Chen, Y.; Hoi, I. -C.; Jeffrey, E.; Kelly, J.; Mutus, J. Y.; O’Malley, P. J. J.; Neill, C.; Roushan, P.; Sank, D.; Vainsencher, A.; Wenner, J.; White, T. C.; Cleland, A. N.; Martinis, J. M. Characterization and Reduction of

- Microfabrication-Induced Decoherence in Superconducting Quantum Circuits. *Appl. Phys. Lett.* **2014**, *105* (6), 062601. <https://doi.org/10.1063/1.4893297>.
- (37) Ahn, Y.; Kim, J.; Ganorkar, S.; Kim, Y. -H.; Kim, S. -I. Thermal Annealing of Graphene to Remove Polymer Residues. *Mater. Express* **2016**, *6* (1), 69–76. <https://doi.org/10.1166/mex.2016.1272>.
- (38) Ahmed, F.; Heo, S.; Yang, Z.; Ali, F.; Ra, C. H.; Lee, H. -I.; Taniguchi, T.; Hone, J.; Lee, B. H.; Yoo, W. J. Dielectric Dispersion and High Field Response of Multilayer Hexagonal Boron Nitride. *Adv. Funct. Mater.* **2018**, *28* (40), 1804235. <https://doi.org/10.1002/adfm.201804235>.
- (39) Lee, B. H.; Cho, Y. H.; Lee, H.; Lee, K. -D.; Kim, S. H.; Sung, M. M. High-Resolution Patterning of Aluminum Thin Films with a Water-Mediated Transfer Process. *Adv. Mater.* **2007**, *19* (13), 1714–1718. <https://doi.org/10.1002/adma.200601884>.
- (40) Cueva, P.; Hovden, R.; Mundy, J. A.; Xin, H. L.; Muller, D. A. Data Processing for Atomic Resolution Electron Energy Loss Spectroscopy. *Microsc. Microanal.* **2012**, *18* (4), 667–675. <https://doi.org/10.1017/S1431927612000244>.

CHAPTER FIVE

Future Directions and Perspectives

5.1. Future Directions

Two-dimensional materials have been under the spotlight for the past decade and have led to the discoveries and demonstrations of numerous exciting new physics and technologies. However, one of the most important questions about 2D materials — *i.e.*, what practical applications would 2D materials offer to science and technology in the future? — has only been partially answered. In this Chapter, my perspective on this question is presented.

First, for fundamental science, 2D materials have been and will continue to be one of the most powerful platforms to explore low-dimensional physics, a central topic in physics since the last century. Recent discovery of 2D monolayer superconductors, magnets (*e.g.* CrI₃¹) and topological insulators (*e.g.* WTe₂) would further allow more complex heterostructures to be built for studies of more complex physics and material structures. From this point of view, 2D materials should play an important role in fundamental science for a long time into the future.

On the contrary, 2D materials have not yet played the same critical role in the technological aspect to date. While technological applications of 2D materials were intensely researched and demonstrated, improvement in existing technologies using 2D materials, such as photovoltaic and sensing, has not provided competitive alternatives to the modern silicon technology. With the large investment of the industry in silicon technology, it is unlikely that 2D materials can replace modern technology in the industry, at least at this point. Nonetheless, 2D materials might be extremely important in future technologies in two different ways.

The first scenario is the integration of 2D materials with modern silicon

technology for additional functionality or a new process. For instance, one can fabricate a 2D material device complementary to a silicon-based device and then integrate them at the end of the fabrication process by transferring 2D material devices at a relatively low temperature (, usually below 200°C). This process is enabled by the unique van der Waals nature of 2D materials. For other materials, it would be difficult due to the growth constraints such as high growth temperature and/or chemical bonding. Another example is using 2D material as a new fabrication tool. As recently demonstrated, graphene, when placed as a spacer, can physically isolate the chemical bonding between the materials grown on the substrates, and yet is thin enough to allow interaction for epitaxial growth². Therefore, it could allow materials to be epitaxially grown on a template substrate, after which they can be easily separated from the growth substrate and transferred to other surfaces. These unique properties and process compatibility of 2D materials with modern technologies are promising aspects where 2D material could lead to technological improvement.

The second important application of 2D materials is their use for the emergent technologies, to which this dissertation is dedicated. Modern technologies are mostly fabricated using a sequential, surface process, where each layer of a device is fabricated on top of the last layer. Compatibility between the layers thus constraints the possible device structures. In contrast, 2D materials could enable a modular fabrication process. Here, each component is fabricated independently and assembled into a device at the end, which can reduce the constraints in device structure. Their atomic thickness and the layer-by-layer assembly process further enables atomic scale designability for these components. Such modular fabrication process with atomic scale designability is especially advantageous for fabricating quantum electronics, because the device architecture needs to be precisely controlled at a few or even sub-nanometer scale. One of the examples is the MoS₂ superconducting qubit

demonstrated in Chapter 4. Here, the device parameters such as the Josephson energy can be readily tuned as a function of the number of layers of MoS₂ in the tunnel barrier, which is much more difficult to achieve with conventional AlO_x barrier. Exploring the use of 2D materials in emergent technologies are, from my perspective, the most important milestone for 2D materials research in technological applications. Chapter 4 is one of such explorations. In the rest of this Chapter, some other ongoing and future works I was involved to achieve this important application of 2D materials will be briefly discussed.

5.2. Ongoing Works

Two-dimensional polymer for Layer-by-Layer Assembly (Science, 2019³)

In this work led by Yu Zhong and Baorui Cheng, we report the synthesis of two-dimensional porphyrin polymer (2DP) films, which have the ultimate limit of monolayer thickness and exhibit wafer-scale homogeneity. These 2DP polymers are synthesized at the sharp pentane/water interface, where the porphyrin monomers are injected into with Laminar flow and precisely controlled concentrations (Figure 5.1a). This Laminar assembly polymerization (LAP) of porphyrin monomers could form monolayers of metal-organic frameworks with Cu²⁺ linkers or covalent organic frameworks with terephthalaldehyde linkers.

The LAP synthesis offers several advantages important for thin-film processing and the integration of 2DP monolayers. First, the growth can be easily scaled up by injecting monomers for a longer time (for larger length) and by adding an array of nozzles in parallel (for larger width). For example, the 2-inch films shown in Figure 5.2b were synthesized with three nozzles in a 2" by 5" reactor. Second, lateral heterojunctions of monolayer 2DPs can be grown with tunable compositions and widths by introducing different monomers from each nozzle and by controlling the

relative injection rates. Finally, the 2DP monolayer films were compatible with the transfer techniques for 2D materials. Therefore, they can be further integrated with 2D materials to form hybrid van der Waals superlattices. One such superlattice was produced by repeatedly stacking in vacuum with a repeating unit of 2DP/3L-MoS₂, as demonstrated in the cross-sectional annular dark field scanning transmission electron microscope image in Figure 5.3c. This demonstration here shows that these new 2DP polymers offer a new genre of building block for the vdW hybrid heterostructures. Since the properties of these 2DPs can be varied by using different linkers/monomers, the addition of these 2DPs to the 2D material family will enable more complex

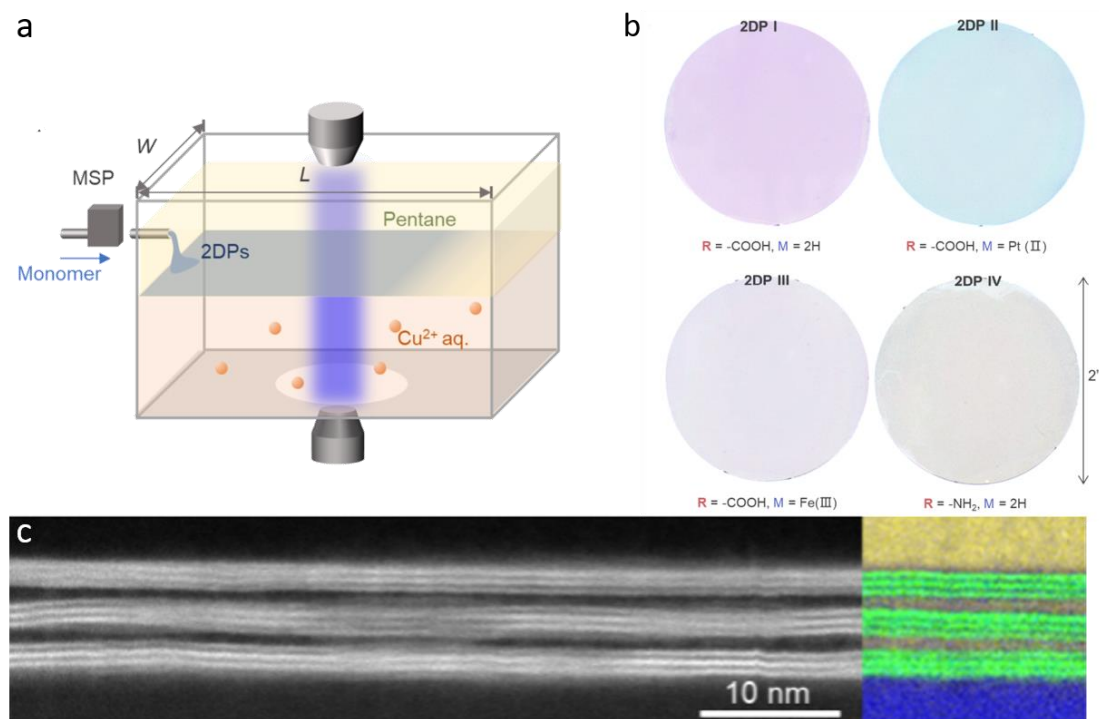


Figure 5.1 Laminar assembly polymerization and hybrid heterostructures. **a**, schematic of a LAP reactor and *in situ* optical characterization apparatus. MSP stands for micro-syringe pump. **b**, false color images of monolayer 2DPs covering entire 2-inch fused silica wafers. **c**, (left) cross-sectional ADF STEM image of a 2DP/(MoS₂)₃ superlattice film transferred onto a SiO₂/Si substrate. Each bright band consists of three MoS₂ monolayers and each dark layer between the bands is a monolayer 2DP. Right: a composite image of carbon (Yellow) and oxygen (Blue) EELS mapping and ADF STEM signal (Green) taken from a different area on the sample. [Figures from Ref³.]

heterostructures, where each layer can be designed to have specific properties for the applications.

Foldable 3D Integrated Atomically-Thin Circuitry

The stiffness of a material is proportional to the cube of the thickness, and

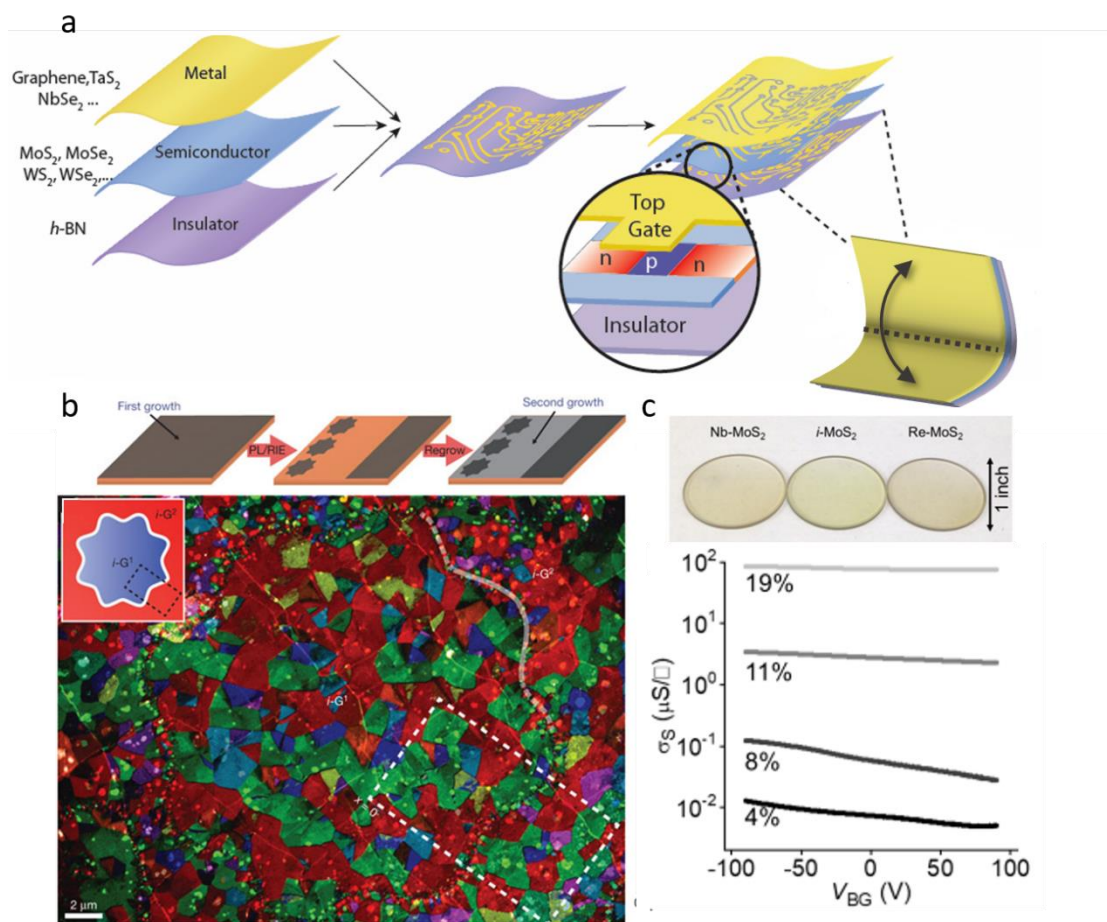


Figure 5.2 Foldable 3D integrated atomically-thin circuitry. **a**, schematics of foldable 3D integrated atomically-thin circuitry. **b**, (top) schematics of patterned-regrowth for graphene-graphene lateral heterostructures. (bottom) Dark-field TEM image of a graphene-graphene lateral heterostructure showing the well-stitched boundary. (inset) Schematics of the pattern of the heterostructure. Reproduced from Ref. 3. **c**, (top) monolayer MoS₂ with different dopants. Samples are grown on a 1" fused silica wafer. Nb is the p-dopant and Re is the n-dopant for MoS₂. (bottom) sheet conductance of MoS₂ monolayer with different Nb doping concentration. [Figure from Ref⁴ and Hui Gao.]

hence to fold a material into smaller dimensions will require it to be thinner. The atomic thickness of 2D materials presents the ultimate minimum that can be obtained. Moreover, 2D materials have been demonstrated to form well-connected lateral heterostructures by patterned-regrowth method (*e.g.* graphene-graphene and graphene-hBN, Figure 5.2b and Ref⁴), which would enable the fabrication of functional circuitry on a monolayer (Figure 5.2a, middle). The PVS process can further allow these functional monolayer circuits to be stacked in the vertical direction, extending the complexity of the circuits into the third dimension (Figure 5.2a, right). As each layer is atomically thin, even after ten circuit layers are assembled, the thickness can still be well below 10 nm. Therefore, the circuits remain extremely foldable. With these circuits, one might be able to fold them into nano-robots that contain functioning electronics to respond to their surroundings.

One challenge toward this foldable 3D integrated atomically-thin circuitry is the limited number of available materials for building the electronics. Modern electronic devices usually includes metal, insulator and various semiconductors. The doping level of the semiconductors (*e.g.*, n- or p-type, degenerate doping) can be precisely, continuously controlled to meet the need for the target functions. In a recent work led by Hui Gao, we developed a substitutional doping method with our metal-organic chemical vapor deposition growth of TMD monolayers (Figure 5.2.c). This method allows us to make MoS₂ into n- or p-type as well as vary their conductivity, which would offer a new component for building the functional atomically thin circuitry to realize the nano-robots.

High Coherence MoS₂ Quantum Electronics

While we have demonstrated the first MoS₂ superconducting qubits in Chapter 4, the estimated coherence time of 12 nanoseconds of the qubit is insufficient for coherent quantum operations. Improving the fabrication process should significantly improve the coherence time similar to the case of AlO_x qubit. The first measured coherence time of the AlO_x qubit is as short as 1 ns, while it is now improved to achieve up to ~100 μs. The improved TMD qubits could potentially lead to two very important applications. First, a MoS₂ qubit could theoretically show a better coherence time than that of a conventional AlO_x qubit. This is because the number of defects in the qubit is the major source of decoherence, and polycrystalline MoS₂ is expected to have fewer defects than the amorphous AlO_x. However, other factors of decoherence are unclear for MoS₂ qubits and could eventually limit the coherence time of MoS₂ qubit. The second application is the studies of microwave properties of 2D materials. While the electrical, optical and mechanical properties of 2D materials are intensively studied, the microwave properties of 2D materials are largely unexplored. For example, the microwave loss tangent of 2D material monolayers at low temperature, single photon power has not been reported. In addition, it has been demonstrated in AlO_x qubit that coherent microwave measurement can be used to probe and characterize the charged defects in the AlO_x⁵, which would be an exciting way to study the defect characteristics in 2D materials.

5.3. Final Thoughts

The field of 2D materials has thrived for years and has achieved many exciting

scientific milestones. In fundamental science, 2D materials provide an indispensable platform to study the important topics of low-dimensional physics. In technological applications, however, 2D materials have yet to demonstrate the same level of impact — partially because the modern silicon technology has performed outstandingly, such as the striking 5 nm-node transistors by Taiwan Semiconductor Manufacturing Company that is coming in the next year. As such, I believe technological demonstrations of 2D materials beyond what silicon technology can achieve is the most critical milestone in the future. The work presented in this dissertation ultimately served two purposes for this: for one, we offered methods that would enable scaling up of exciting future demonstrations; for the other, we offer a method to use 2D materials to explore their applications in the superconducting quantum computers, which is an example of technologies beyond modern silicon technology. I sincerely hope the results discussed here — six and a half years of hard work — would one day pave the way for future 2D material-based technologies that could eventually improve human life.

5.4. Reference

1. Huang, B., Clark, G., Navarro-Moratalla, E., Klein, D. R., Cheng, R., Seyler, K. L., Zhong, D., Schmidgall, E., McGuire, M. A., Cobden, D. H., Yao, W., Xiao, D., Jarillo-Herrero, P. & Xu, X. Layer-dependent ferromagnetism in a van der Waals crystal down to the monolayer limit. *Nature* **546**, 270–273 (2017).
2. Kim, Y., Cruz, S. S., Lee, K., Alawode, B. O., Choi, C., Song, Y., Johnson, J. M., Heidelberg, C., Kong, W., Choi, S., Qiao, K., Almansouri, I., Fitzgerald, E. A.,

- Kong, J., Kolpak, A. M., Hwang, J. & Kim, J. Remote epitaxy through graphene enables two-dimensional material-based layer transfer. *Nature* **544**, 340–343 (2017).
3. Zhong, Y., Cheng, B., Park, C., Ray, A., Brown, S., Mujid, F., Lee, J.-U., Zhou, H., Suh, J., Lee, K.-H., Mannix, A. J., Kang, K., Sibener, S. J., Muller, D. A. & Park, J. Wafer-scale synthesis of monolayer two-dimensional porphyrin polymers for hybrid superlattices. *Science* eaax9385 (2019). doi:10.1126/science.aax9385
 4. Levendorf, M. P., Kim, C.-J., Brown, L., Huang, P. Y., Havener, R. W., Muller, D. A. & Park, J. Graphene and boron nitride lateral heterostructures for atomically thin circuitry. *Nature* **488**, 627–632 (2012).
 5. Klimov, P. V., Kelly, J., Chen, Z., Neeley, M., Megrant, A., Burkett, B., Barends, R., Arya, K., Chiaro, B., Chen, Y., Dunsworth, A., Fowler, A., Foxen, B., Gidney, C., Giustina, M., Graff, R., Huang, T., Jeffrey, E., Lucero, E., Mutus, J. Y., Naaman, O., Neill, C., Quintana, C., Roushan, P., Sank, D., Vainsencher, A., Wenner, J., White, T. C., Boixo, S., Babbush, R., Smelyanskiy, V. N., Neven, H. & Martinis, J. M. Fluctuations of Energy-Relaxation Times in Superconducting Qubits. *Phys. Rev. Lett.* **121**, 090502 (2018).